Postmerger Mass Ejection of Low-mass Binary Neutron Stars

Sho Fujibayashi[1] , Shinya Wanajo[1,2,3] , Kenta Kiuchi[1,4] , Koutarou Kyutoku[3,4,5] , Yuichiro Sekiguchi[4,6] , and Masaru Shibata[1,4]

[1] Max-Planck-Institut für Gravitationsphysik (Albert-Einstein-Institut), Am Mühlenberg 1, D-14476 Potsdam-Golm, Germany; sho.fujibayashi@aei.mpg.de
[2] Department of Engineering and Applied Sciences, Faculty of Science and Technology, Sophia University, 7-1 Kioicho, Chiyoda-ku, Tokyo, 102-8554, Japan
[3] Interdisciplinary Theoretical and Mathematical Science (iTHEMS) Research Group, RIKEN, Wako, Saitama, 351-0198, Japan
[4] Center for Gravitational Physics, Yukawa Institute for Theoretical Physics, Kyoto University, Kyoto, 606-8502, Japan
[5] Department of Physics, Kyoto University, Kyoto, 606-8502, Japan
[6] Department of Physics, Toho University, Funabashi, Chiba, 274-8510, Japan
Received 2020 June 10; revised 2020 July 30; accepted 2020 August 14; published 2020 September 29

Abstract

We study the postmerger mass ejection of low-mass binary neutron stars (NSs) with the system mass of $2.5\,M_\odot$ and subsequent nucleosynthesis by performing general-relativistic, neutrino-radiation viscous-hydrodynamics simulations in axial symmetry. We find that the merger remnants are long-lived massive NSs surviving more than several seconds, irrespective of the nuclear equations of state (EOSs) adopted. The ejecta masses of our fiducial models are ~ 0.06–$0.1\,M_\odot$ (depending on the EOS), being $\sim 30\%$ of the initial disk masses (~ 0.15–$0.3\,M_\odot$). Postprocessing nucleosynthesis calculations indicate that the ejecta is composed mainly of light r-process nuclei with small amounts of lanthanides (mass fraction ~ 0.002–0.004) and heavier species due to the modest average electron fraction (~ 0.32–0.34) for a reasonable value of the viscous coefficient. Such abundance distributions are compatible with those in weak r-process stars such as HD 122563 but not with the solar r-process-like abundance patterns found in all measured r-process-enhanced metal-poor stars. Therefore, low-mass binary NS mergers should be rare. If such low-mass NS mergers occur, their electromagnetic counterparts, kilonovae, will be characterized by an early bright blue emission because of the large ejecta mass as well as the small lanthanide fraction. We also show, however, that if the effective turbulent viscosity is very high, the electron fraction of the ejecta could be low enough that the solar r-process-like abundance pattern is reproduced and the lanthanide fraction becomes so high that the kilonova would be characterized by early bright blue and late bright red emissions.

Unified Astronomy Thesaurus concepts: Gravitational wave sources (677); Nucleosynthesis (1131); R-process (1324); Neutron stars (1108); High energy astrophysics (739)

1. Introduction

Binary neutron star (NS) mergers are characterized by the following astrophysical aspects. First, they are the sources of gravitational waves that can be detected by ground-based gravitational-wave detectors (Abadie et al. 2010; Accadia et al. 2011; Akutsu et al. 2018). Second, the remnant of an NS merger, that is, either the massive NS or black hole (BH) surrounded by an accretion disk, could be a central engine of short gamma-ray bursts (e.g., Eichler et al. 1989), for which the afterglow follows later on across a wide range of electromagnetic wavelengths (from X-rays to radio, Metzger & Berger 2012; Hotokezaka & Piran 2015, and references therein). Third, NS mergers are promising sites for nucleosynthesis for about half of the elements heavier than iron—the rapid neutron capture (r-process) nuclei (Lattimer & Schramm 1974; Symbalisty & Schramm 1982; Eichler et al. 1989; Meyer 1989; Freiburghaus et al. 1999; see also a recent comprehensive review, Cowan et al. 2019). The decaying radioactive nuclei freshly synthesized in the merger ejecta release energy and power an ultraviolet-optical-infrared transient called a kilonova or macronova (Li & Paczyński 1998; Kulkarni 2005; Metzger et al. 2010). All of these (gravitational- and electromagnetic-wave) signals have been observed in the first gravitational-wave event from the binary NS merger GW170817 (Abbott et al. 2017a, 2017b; Alexander et al. 2017; Villar et al. 2017; Lyman et al. 2018), while in the second binary NS merger event, GW190425 (Abbott et al. 2020), no electromagnetic counterpart has been detected. This indicates that there is a wide variety of possibilities in binary NS mergers reflected by the variation of system masses (the inferred values are 2.73–2.78 $M_\odot$ for GW170817 and $\sim 3.4\,M_\odot$ for GW190425).

The merger of binary NSs is accompanied by successive mass-ejection episodes as found in recent general-relativistic hydrodynamical simulations including weak interactions as well as temperature-dependent nuclear equations of state (EOSs; e.g., Shibata & Hotokezaka 2019). During the merger stage, the so-called dynamical mass ejection occurs, and material of $\sim 10^{-3}$–$10^{-2}\,M_\odot$ is ejected by tidal torque and shock heating (e.g., Bauswein et al. 2013; Hotokezaka et al. 2013; Palenzuela et al. 2015; Sekiguchi et al. 2015, 2016; Foucart et al. 2016; Bovard et al. 2017; Shibata et al. 2017a; Radice et al. 2018; Vincent et al. 2020). The resultant wide range of electron fractions, $Y_e \sim 0.1$–0.4, in the ejecta generally leads to the robust production of r-process nuclei with an abundance pattern that agrees reasonably with the solar r-process abundance distribution as shown by nucleosynthesis studies (Wanajo et al. 2014; Goriely et al. 2015; Bovard et al. 2017; Radice et al. 2018).

The postmerger mass-ejection phase then follows for seconds, during which about 10%–50% of the material in the accretion disk (~ 0.01–$0.1\,M_\odot$) around the central remnant becomes unbound by viscous heating (here the viscosity is believed to originate from magnetorotational instability, MRI; e.g., Fernández & Metzger 2013; Just et al. 2015;

Fujibayashi et al. 2018; Siegel & Metzger 2018; Fernández et al. 2019).[7] The central remnant can be either a (hyper) massive NS or a BH depending primarily on the total mass of the binary NSs as well as the nuclear EOS. In the case where the total mass is larger than a certain critical value determined for a given EOS, the merger remnants collapse into a BH promptly or after the phase of a short-lived hypermassive NS (Shibata & Taniguchi 2006; Shibata & Hotokezaka 2019).

In the BH accretion disk, the viscous effect heats up the material and transports the angular momentum outward in the accretion disk, leading eventually to mass ejection from the disk. The viscous heating generates thermal energy that induces the electron–positron pair creation, enhancing the positron capture by neutrons and increasing the electron fraction, $Y_{\rm e}$. The viscous expansion reduces the density of the disk material, and as a result, the electron degeneracy is decreased, increasing $Y_{\rm e}$ as well (at this stage, the role of neutrino irradiation on varying $Y_{\rm e}$ is subdominant). However, the average values of $Y_{\rm e}$ for the ejecta, $\langle Y_{\rm e} \rangle$, show some diversity in the literature: $\langle Y_{\rm e} \rangle \sim 0.1$–$0.2$ (Fernández & Metzger 2013; Siegel & Metzger 2018; Fernández et al. 2019), $\langle Y_{\rm e} \rangle \sim 0.2$–$0.3$ (Just et al. 2015; Miller et al. 2019), and $\langle Y_{\rm e} \rangle \sim 0.3$ (Fernández et al. 2020; Fujibayashi et al. 2020). Accordingly, the nucleosynthesis outcomes differ from those of each other.

In the case where the total mass of binary NSs is smaller than a critical value, which is the main focus of this paper, a long-lived massive NS is formed, and it emits copious neutrinos that further increase the value of $Y_{\rm e}$ in the ejecta. The average values of $Y_{\rm e}$ for the ejecta derived in numerical simulations are in reasonable agreement among different groups, $\langle Y_{\rm e} \rangle \sim 0.3$–$0.4$ (for the lifetimes of massive NSs longer than a few 100 ms). However the number of such works is still limited (Metzger & Fernández 2014; Perego et al. 2014; Lippuner et al. 2017; Fujibayashi et al. 2018). Moreover, the numerical methods are rather different among these work. In Metzger & Fernández (2014), Perego et al. (2014), and Lippuner et al. (2017), the central massive NS is not solved self-consistently. By contrast, Fujibayashi et al. (2018) self-consistently evolved the post-merger system (both the remnant NS and disk around it) by adopting the 3D result of the dynamical phase of an equal-mass (1.35 $M_\odot$) NS merger (Sekiguchi et al. 2015, 2016) as the initial condition.

The resultant nucleosynthetic abundance distributions in the postmerger ejecta from such systems exhibit a pattern that is different from the solar r-process pattern, with small amounts of heavy r-process nuclei. This is due to the modest neutron richness of the ejected material. Such r-process abundance patterns predicted from the above simulations for long-lived massive NSs disagree with the implication from the spectroscopic analyses of Galactic halo stars. To date, all measured r-process-enhanced stars appear to exhibit solar r-process-like abundance patterns, in particular for the range of atomic number $Z = 56$–78 (Ba–Pt, e.g., Cowan et al. 2019), although few measurements of the second r-process peak (Te, $Z = 52$, only available from space) have been reported (Roederer et al. 2012a). Deviation from the solar r-process pattern, which can be seen for $Z = 38$–47 (Sr–Ag), is generally not larger than a factor of a few.

However, the discovery of the lowest-mass double-NS system to date, PSR J1946+2052 (Stovall et al. 2018), strongly

suggests the presence of long-lived massive NSs as merger remnants. The system mass of J1946+2052 is only $2.50 \pm 0.04\,M_\odot$, substantially smaller than the typical value of ~ 2.6–$2.7\,M_\odot$ for the observed Galactic double-NS systems (e.g., Tauris et al. 2017) and those inferred for the NS mergers GW170817 (2.73–$2.78\,M_\odot$; Abbott et al. 2017a) and GW190425 ($\sim 3.4\,M_\odot$; Abbott et al. 2020). Thus, the long-lived (possibly supramassive) NSs surrounded by accretion disks could be the outcomes for this class of binary NS mergers.

The purpose of this work is to study the mass ejection and subsequent nucleosynthesis for the postmerger of low-mass NS binaries near the low-mass end. The paper is organized as follows. In Section 2 we summarize our fully general-relativistic, neutrino-radiation, and viscous-hydrodynamics code. The system mass is taken to be 2.5 $M_\odot$ (and 2.7 $M_\odot$ for comparison purposes), being similar to that of J1946+2052. We consider an equal-mass case; each NS mass is 1.25 $M_\odot$ (and 1.35 $M_\odot$) because the mass ratio of two NSs in this case is likely close to unity due to the lower bound of NS mass, $\sim 1.2\,M_\odot$, predicted from theoretical studies (Müller 2016; Suwa et al. 2018). Two temperature-dependent nuclear EOSs, DD2 (Banik et al. 2014) and SFHo (Steiner et al. 2013), are adopted in the simulations. In Section 3, the hydrodynamical outcomes are discussed. The properties of the central massive NS, disk, and ejecta that are important for the nucleosynthesis are shown. In particular, we describe how the electron fraction of the ejecta is determined by considering the timescales of the weak-interaction processes. The thermodynamic histories extracted from each simulation by several thousand tracer particles are then used for nucleosynthesis calculations (Section 4). The time variations of radioactive energies, which power kilonova emission, are also obtained from the nucleosynthesis calculations. Finally, we present the summary and conclusions of our study in Section 5. Throughout this paper, we employ the geometrical units in which the speed of light c and gravitational constant G are set to unity.

2. Method

2.1. Einstein's Equation

We use a fully general-relativistic, neutrino-radiation, viscous-hydrodynamics code developed in our previous work (Fujibayashi et al. 2018). Einstein's equation is solved with a version of the puncture-Baumgarte–Shapiro–Shibata–Nakamura (BSSN) formalism (Shibata & Nakamura 1995; Baumgarte & Shapiro 1999; Marronetti et al. 2008) incorporating the Z4c prescription (Hilditch et al. 2013) for the constraint violation propagation. The quantities solved in this formalism are listed in Table 1. From the three-metric γ_{ij} and extrinsic curvature K_{ij}, we define $\tilde{\gamma}_{ij} = \gamma^{-1/3}\gamma_{ij}$, $W = \gamma^{-1/6}$, $K = \gamma^{ij}K_{ij}$, $\tilde{A}_{ij} = \gamma^{-1/3}(K_{ij} - \gamma_{ij}K/3)$, and $F_i = \delta^{jk}\partial_j\tilde{\gamma}_{ik}$. Here γ denotes the determinant of γ_{ij} and the determinant of $\tilde{\gamma}_{ij}$ is assumed to be unity. For the gauge conditions, we employ the dynamical lapse and shift gauge conditions described in Equations (1) and (2) in Fujibayashi et al. (2017). We introduce a new variable Θ, which indicates the degree of constraint violation, for constraint propagation in the Z4c formalism (Hilditch et al. 2013). For this change, the equations in the original BSSN formalism are slightly modified. For example, $\hat{K} \equiv K - 2\Theta$ obeys the same evolution equation as K (see, for example, Shibata 2016). We

---

[7] We note that the neutrino drag effect may suppress the growth of MRI (Guilet et al. 2017).

Table 1
List of the Quantities Evolved in Our Formalism

Notation	Definition	Reference
$\tilde{\gamma}_{ij} = \gamma^{-1/3}\gamma_{ij}$	Conformal three-metric	Shibata & Nakamura (1995)
$W = \gamma^{-1/6}$	Conformal factor	Marronetti et al. (2008)
$K = \gamma^{ij}K_{ij}$	Trace of the extrinsic curvature K_{ij}	Shibata & Nakamura (1995)
$\tilde{A}_{ij} = \gamma^{-1/3}(K_{ij} - \gamma_{ij}K/3)$	Trace-free part of K_{ij}	Equation (2.9) in Shibata & Nakamura (1995)
$F_i = \delta^{jk}\partial_j\tilde{\gamma}_{ki}$	Auxiliary variable	Equation (2.19) in Shibata & Nakamura (1995)
Θ	Hamiltonian constraint violation	Hilditch et al. (2013)

write the evolution equation of Θ as

$$(\partial_t - \beta^k\partial_k)\Theta = \frac{1}{2}\alpha\left[R - \tilde{A}_{ij}\tilde{A}^{ij} \right. $$
$$\left. + \frac{2}{3}(\hat{K} + 2\Theta) - 16\pi\rho_h\right]e^{-r^2/r_o^2}, \quad (1)$$

where $\rho_h \equiv T^{\alpha\beta}n_\alpha n_\beta$, $r = \sqrt{x^2 + y^2 + z^2}$, and $r_o \approx 1000\,\text{km}$. Here we set $\kappa_1 = \kappa_2 = 0$ in the full description of Z4c in Hilditch et al. (2013). As Equation (1) shows, we incorporate the constraint propagation only for a near zone to avoid the accumulation of the constraint violation only in the strong field zone.

We adopt the sixth-order Kreiss–Oliger dissipation for all the geometrical variables except for the lapse function to avoid the numerical instability that could appear when employing a nonuniform grid in the numerical evolution. We solve Einstein's evolution equation in Cartesian coordinates and employ the so-called cartoon method to impose axisymmetric conditions for the geometrical quantities (Shibata 2000; Alcubierre et al. 2001). In this paper, we employ the fourth-order Lagrangian interpolation for the cartoon procedure as in the series of our recent papers (e.g., Fujibayashi et al. 2018, 2020).

2.2. Radiation Viscous-hydrodynamics Equations

We briefly describe the basic equations and our method to solve viscous-hydrodynamics equations with neutrino radiation transfer. We solve the following evolution equations in a two-dimensional (2D) axisymmetric manner. We decompose neutrinos into "streaming" and "trapped" components. Then we also decompose the total energy-momentum tensor of the matter, which includes fluid and neutrinos, as

$$T^{\alpha\beta}_{(\text{tot})} = T^{\alpha\beta} + \sum_i T^{\alpha\beta}_{(\nu_i, S)}, \quad (2)$$

where $T^{\alpha\beta}$ is the sum of the energy-momentum tensors for the fluid $T^{\alpha\beta}_{(\text{fluid})}$ and trapped neutrinos $T^{\alpha\beta}_{(\nu_i, T)}$, and $T^{\alpha\beta}_{(\nu_i, S)}$ is that for streaming neutrinos. The index i specifies the neutrino species. Following our previous work (Fujibayashi et al. 2017, 2018), we consider three species of neutrinos: electron neutrinos ν_e, electron antineutrinos $\bar{\nu}_e$, and the other neutrino species ν_x, which represents muon and tau neutrinos and those antineutrinos altogether.

The evolution equations for these energy-momentum tensors are

$$\nabla_\beta T^{\alpha\beta} = -Q^\alpha_{(\text{leak})} = -\sum_i Q^\alpha_{(\text{leak})\nu_i}, \quad (3)$$

$$\nabla_\beta T^{\alpha\beta}_{(\nu_i, S)} = Q^\alpha_{(\text{leak})\nu_i}, \quad (4)$$

where $Q^\alpha_{(\text{leak})\nu_i}$ denotes the "leakage" rate of the ith species of neutrinos. Note that this leakage rate includes the heating due to neutrino absorption and pair annihilation, as well as the cooling due to neutrino emission, as described in Fujibayashi et al. (2017).[8] To solve the evolution equations for streaming neutrinos, we employ Thorne's truncated moment formalism (Thorne 1981; Shibata et al. 2011a) with a closure relation (Levermore 1984; González et al. 2007). For trapped neutrinos, we employ a leakage-based scheme developed in Sekiguchi (2010). The detailed description of these schemes is found in Sekiguchi (2010) and Fujibayashi et al. (2017).

The energy-momentum tensor of a viscous fluid with trapped neutrinos is written as

$$T_{\alpha\beta} = \rho h u_\alpha u_\beta + P g_{\alpha\beta} - \rho h \nu \tau^0_{\alpha\beta}, \quad (5)$$

where ρ is the baryon rest-mass density, $h = 1 + \varepsilon + P/\rho$ is the specific enthalpy with the specific internal energy ε and the pressure P, u^α is the four-velocity of the fluid, ν is the viscous coefficient, and $\tau^0_{\alpha\beta}$ is a shear viscous stress tensor, which is a symmetric tensor satisfying the relation $\tau^0_{\alpha\beta}u^\alpha = 0$.

Following Israel & Stewart (1979), we write the evolution equation for the viscous stress tensor as

$$\mathcal{L}_u\tau^0_{\alpha\beta} = -\zeta(\tau^0_{\alpha\beta} - \sigma_{\alpha\beta}), \quad (6)$$

with the shear tensor $\sigma_{\alpha\beta}$ defined by

$$\sigma_{\alpha\beta} = h_\alpha{}^\mu h_\beta{}^\nu(\nabla_\mu u_\nu + \nabla_\nu u_\mu) = \mathcal{L}_u h_{\alpha\beta}. \quad (7)$$

Here, $h_{\alpha\beta} = g_{\alpha\beta} + u_\alpha u_\beta$. ζ is a nonzero constant of (time)$^{-1}$ dimension, which is set to $3 \times 10^4\,\text{rad s}^{-1}$ in this work following our previous work (Fujibayashi et al. 2018). The value is approximately four times larger than the largest angular velocity of the system, $\approx 7000\,\text{rad s}^{-1}$. With this

---

[8] We updated the electron and positron capture rates from those originally described in Sekiguchi (2010). Previously, we used the difference of the chemical potential of protons and neutrons as the Q value in calculating those rates, while in the current work, the mass difference between neutrons and protons is used for this. After this update, we calibrated the neutrino luminosity derived in our simulation for the core collapse of a $15\,M_\odot$ solar-metallicity progenitor (Woosley et al. 2002) by comparing with that in Liebendörfer et al. (2003) and Janka et al. (2012) to appropriately set the parameters of our leakage-based neutrino radiation transport method (see Sekiguchi 2010 for the parameters). Then, we performed 3D merger simulations again using the calibrated parameters. We found that our previous prescription gives higher values of the electron fraction in the equilibrium of weak-interaction reactions. This led to an overestimation of the electron fraction of the ejecta in previous works (Sekiguchi et al. 2015, 2016; Fujibayashi et al. 2018), typically by ~ 0.05. Our previous prescription also overestimated the dynamical ejecta mass as $\approx 0.011 M_\odot$, which is $\sim 30\%$ larger than that in this study (for SFHo-135; see Table 2).

Table 2
List of Models for the Three-dimensional Merger Simulation

Model	EOS	M_{NS} ($M_\odot$)	R_{cold} (km)	$t_{end}-t_{merge}$ (ms)	M_{ej} ($10^{-2}M_\odot$)	$\langle V_{ej}\rangle$ (c)	$\langle s_{ej}\rangle$ (k_B)	$\langle Y_{e,ej}\rangle$	N_{tp}	X_{la}
DD2-125	DD2	1.25	13.14	48.5	0.10	0.19	27	0.20	2203	0.17
SFHo-125	SFHo	1.25	11.96	50.8	0.13	0.18	21	0.27	2511	0.072
DD2-135	DD2	1.35	13.18	61.7	0.15	0.19	25	0.23	2761	0.093
SFHo-135	SFHo	1.35	11.92	66.6	0.83	0.27	16	0.24	2197	0.031

Note. M_{NS}, R_{cold}, $t_{end}-t_{merge}$, M_{ej}, $\langle V_{ej}\rangle$, $\langle s_{ej}\rangle$, $\langle Y_{e,ej}\rangle$, N_{tp}, and X_{la} are the mass of each NS, radius of the cold spherical NS with the mass of M_{NS}, time after merger at which the simulation is terminated, ejecta mass, their average velocity, entropy, and electron fraction, the number of tracer particles we used, and the mass fraction of lanthanides, respectively. The ejecta is defined as the material that satisfies Equation (10).

prescription, the tensor $\tau^0_{\alpha\beta}$ approaches the shear tensor $\sigma_{\alpha\beta}$ in a sufficiently short timescale of $\sim\zeta^{-1} \approx 0.03$ ms.

We can rewrite Equation (6) as

$$\mathcal{L}_u\tau_{\alpha\beta} = -\zeta\tau^0_{\alpha\beta}, \tag{8}$$

where $\tau_{\alpha\beta} \equiv \tau^0_{\alpha\beta} - \zeta h_{\alpha\beta}$. Thus, in addition to the hydrodynamics equations of Equation (3), we solve Equation (8) as a basic equation that describes the evolution of $\tau_{\alpha\beta}$. The details of the formulation of our general-relativistic viscous-hydrodynamics code are found in Shibata et al. (2017b).

For the viscous coefficient, we use the so-called Shakura–Sunyaev description as

$$\nu = \alpha_{vis}c_s H_{tur}, \tag{9}$$

where c_s is the sound speed and H_{tur} is a typical scale height of the system (Shakura & Sunyaev 1973). We adopt $H_{tur} = 10$ km following Fujibayashi et al. (2018).

2.3. Condition for the Ejecta

To study the property of the ejecta in numerical simulations, we have to identify the unbound material in a finite computational domain. This gives us a nontrivial question about how we should determine the condition for the unbound material. There are several possibilities for this condition. In our previous numerical simulations for binary NS mergers (Sekiguchi et al. 2015, 2016), we employed the condition

$$u_t + 1 < 0 \tag{10}$$

for the entire fluid elements in the computational domain, assuming that the dynamical ejecta has a small internal energy, which is much smaller than the kinetic energy. In our previous axisymmetric simulation for the evolution of the merger remnants (Fujibayashi et al. 2018), we employed the condition

$$hu_t + 1 < 0 \tag{11}$$

for the fluid elements that have outgoing velocity, i.e., we took into account the thermal contribution for identifying the ejecta because the kinetic energy per mass of the postmerger ejecta is much smaller than that of the dynamical ejecta.

In the present work, alternatively, we employ the following condition:

$$hu_t + h_{min} < 0, \tag{12}$$

where h_{min} is the minimum value of the specific enthalpy in the chosen tabulated EOS (≈ 0.9987). The reason for this choice is that the atomic mass unit m_u is used as the mass per baryon in the EOS we employed, and thus, the specific enthalpy can be

smaller than unity for the case where the actual mass per baryon is lighter than m_u and where the pressure contribution to the enthalpy is negligible.

We note that the material with the lowest specific enthalpy h_{min} is composed mainly of heavy nuclei in the EOSs employed in this study, in which nuclear statistical equilibrium (NSE) is assumed for the nuclear composition. Thus, in Equation (12), the energy released by the recombination of free nucleons into heavy nuclei is taken into account. That is, Equation (12) is the condition for the material being unbound only for the case where the temperature of the material is low enough that free nucleons recombine into heavy nuclei. One issue for using Equation (12) is that some fluid components, which stay in the central region and are strongly bounded by the central massive NS, can satisfy this condition. Such components remain composed of free nucleons, and thus, even if the material satisfies Equation (12), it is not ejected eventually. To remove the contribution of this component, we in addition impose the condition of $r \geqslant 500$ km to identify the real ejecta component when we employ Equation (12) as the condition.

Obviously, the total mass of the ejecta becomes largest when we employ Equation (12). Thus, in our previous studies, in particular for the case where we employed Equation (10), the total mass of the ejecta would be underestimated (see Table 2). Also, the property of the ejecta such as the average electron fraction depends weakly on the choice of the condition for the unbound object.

2.4. Initial Condition

As in our previous work (Fujibayashi et al. 2017, 2018), we use hydrodynamical configurations obtained by three-dimensional (3D) numerical relativity simulations for equal-mass binary NS mergers as the initial condition for our 2D simulations. At several tens of milliseconds after the merger, the system, which is composed of a massive NS and an accretion disk, becomes nearly axisymmetric. We averaged the 3D hydrodynamical quantities at ≈ 50 ms after the merger over the azimuthal angle around the rotational axis to obtain a 2D axisymmetric hydrodynamical configuration used in our simulation. For the viscous tensor, we set $\tau^0_{\alpha\beta} = 0$ initially. That is, we assume that the fluid is ideal initially. The initial condition for the geometrical variables is determined in the assumption of conformal flatness for γ_{ij} and by solving the Hamiltonian and momentum constraints for a given matter configuration.

In this work, we set the origin of time $t = 0$ to the beginning of our 2D simulation, which is ≈ 50 ms after the onset of the merger.

Table 3
List of Models for the Two-dimensional Postmerger Simulation

Model	EOS	M_{NS} $(M_\odot)$	Δx_0 (m)	N_{grid}	L (km)	α_{vis}	t_{end} (s)	M_{disk} $(10^{-2}M_\odot)$	$M_{ej,tot}$ $(10^{-2}M_\odot)$	$\langle V_{ej}\rangle$ (c)	$\langle s_{ej}\rangle$ (k_B)	$\langle Y_{e,ej}\rangle$	N_{tp}	X_{la}
DD2-125M	DD2	1.25	200	921	8411	0.04	6.2	32.8 (26.6)	11.4	0.089	15.0	0.322	39808	0.00441
SFHo-125H	SFHo	1.25	160	993	8745	0.04	3.8	14.8 (12.7)	6.1	0.108	18.7	0.342	24576	0.00261
DD2-135M	DD2	1.35	200	921	8411	0.04	6.1	24.8 (21.2)	8.6	0.098	17.3	0.337	39168	0.00276
DD2-125L[a]	DD2	1.25	250	857	8148	0.04	7.6	32.6 (26.3)	10.6	0.089	15.5	0.326	44416	0.00441
DD2-135L[a]	DD2	1.35	250	857	8148	0.04	6.9	24.3 (21.2)	8.5	0.095	18.8	0.346	48768	0.00378
DD2-125M-h[b]	DD2	1.25	200	921	8411	0.10	1.5	35.4 (31.6)	19.8	0.113	13.8	0.282	9856	0.0298
DD2-135M-v14[c]	DD2	1.35	200	921	8411	0.04	2.8	27.9 (23.7)	8.7	0.113	20.4	0.341	⋯	⋯
DD2-135M-irr[d]	DD2	1.35	200	921	8411	0.04	5.6	24.7 (21.1)	6.9	0.106	16.3	0.287	⋯	⋯
DD2-135M-v0[e]	DD2	1.35	200	921	8411	0.00	1.1	40.9 (11.0)	0.3	0.164	21.1	0.262	⋯	⋯

Notes. M_{NS}, Δx_0, N_{grid}, L, α_{vis}, t_{end}, M_{disk}, $M_{ej,tot}$, $\langle V_{ej}\rangle$, $\langle s_{ej}\rangle$, $\langle Y_{e,ej}\rangle$, N_{tp}, and X_{la} are the mass of each NS, the grid spacing of the inner computational region, the grid number in each direction, the size of the computational domain, viscous parameter, time at which the simulation is terminated, initial disk mass, ejecta mass, its average velocity, entropy, electron fraction, the number of tracer particles we used, and the mass fraction of lanthanides, respectively. The initial disk mass is defined as the mass outside the NS radius R_{NS} (see Section 3.2 for its definition) at $t = 10$ ms. In the parentheses, the mass of the material with $\rho < 10^{12}$ g cm^{-3} is shown. For $M_{ej,tot}$, $\langle V_{ej}\rangle$, $\langle s_{ej}\rangle$, and $\langle Y_{e,ej}\rangle$, the values at $t = t_{end}$ are shown.
[a] The model with a lower resolution.
[b] The model with a higher viscous parameter.
[c] The model without viscosity in the region with $\rho > 10^{14}$ g cm^{-3}.
[d] The model without neutrino irradiation.
[e] The model without viscosity.

2.5. 3D Models

In this subsection, we briefly describe models for the 3D merger simulation. The 3D simulations are performed using our numerical relativity code with an approximate neutrino radiation transport (Sekiguchi et al. 2015, 2016). We employ the puncture-BSSN formalism for the evolution of the geometrical quantities and the leakage-based scheme described in Section 2.2 for the neutrino transport. In these 3D simulations, the neutrino absorption is taken into account as the heating source, but not the other processes such as the neutrino pair annihilation.

In this paper, we explore three models with different nuclear EOSs and total masses of the system as shown in Table 2. As mentioned in Section 1, we use two finite-temperature EOSs for nuclear matter, referred to as SFHo (Steiner et al. 2013) and DD2 (Banik et al. 2014), which predict the maximum mass of cold spherical NSs to be $2.06\,M_\odot$ and $2.42\,M_\odot$, respectively. We extend the tables of these EOSs to low-density and low-temperature ranges down to ≈ 0.16 g cm^{-3} and 10^{-3} MeV, respectively, using the EOS of ideal gas with arbitrarily relativistic and degenerate electrons (Timmes & Swesty 2000). We consider the equal-mass binaries with two sets of NS masses, 1.25 and 1.35 $M_\odot$.

In Table 2, the properties of the dynamical ejecta (defined by Equation (10)) are shown. They depend on the total mass of the binary and adopted EOS (Bauswein et al. 2013; Hotokezaka et al. 2013). The SFHo EOS is "softer" than DD2, in the sense that if we compare the radius of the NS with the same gravitational mass, the radius in the SFHo EOS is smaller than that in the DD2. The softer EOS generally enhances the shock-heating efficiency in the early evolution stage of the massive NS, which plays a role in increasing the fraction of unbound material. This leads to a larger ejecta mass for SFHo models than those for DD2 models for equal-mass binary mergers. In addition, the positron capture is enhanced in the shocked ejecta due to its high temperature, and thus the average values of the electron fraction for SFHo models are higher than those for

DD2 models. For DD2 models, the mass ejection is driven predominantly by the tidal effect, which leads to the lower electron fraction of the ejecta. The dynamical mass ejection occurs primarily toward the direction of the equatorial plane, in particular for the low-mass cases, because the tidal effect is the main mass-ejection channel.

We note that the ejecta mass depends on its definition (see Section 2.3). For example, the ejecta mass for model DD2-125 evaluated using the condition given by Equation (12) with $r \geqslant 500$ km is $\approx 0.002\,M_\odot$, which is approximately twice as large as that using the condition Equation (10) ($\approx 0.001\,M_\odot$; see Table 2). On the other hand, the average electron fraction of the ejecta changes only slightly (by less than 5%).

2.6. Setting and Models for 2D Simulation

The models for our 2D simulations in this study are listed in Table 3. For each model, the same EOS tables as those employed in the 3D simulation are used. To evolve the radiation viscous-hydrodynamics equations in the cylindrical coordinates (x, z), we employ the same nonuniform grid as that in our previous work (Fujibayashi et al. 2017, 2018), in which the grid structure is determined by the uniform grid spacing for the inner region (Δx_0), the range of the inner region (R_{star}), the increase rate of the grid spacing for the outer region ($1 + \delta$), and the total grid number in each direction (N_{grid}). For all models in this study, we adopt $R_{star} = 30$ km and $\delta = 0.0075$. We list Δx and N_{grid} for each model, together with the size of the computational domain, L, in Table 3.

Our fiducial models are DD2-125M, SFHo-125H, and DD2-135M. For DD2-125M and DD2-135M, we set $\Delta x_0 = 200$ m. On the other hand, for SFHo-125H, we employ a finer grid resolution with $\Delta x_0 = 160$ m than those in other models, because the stellar radii for the SFHo EOS are smaller than those for the DD2 EOS, and thus, the conservation of the total energy is less satisfied in a lower-resolution model. We also perform several other simulations: lower-resolution ones (DD2-125L and DD2-135L) with $\Delta x_0 = 250$ m in order to confirm

the convergence of the numerical results with the adopted grid resolutions, one without the viscosity in the region for which the density is higher than 10^{14} g cm^{-3} (DD2-135M-v14) to clarify that the viscosity in the innermost region of the NS does not play an important role for the early viscosity-driven ejecta (Section 3.1), one without the viscosity in the whole region (DD2-135M-v0) to examine the effect of the viscosity on the evolution of the remnant and the ejecta, and one without neutrino heating/irradiation in the optically thin region (DD2-135M-irr) to understand the importance of neutrino absorption in the evolution of the remnant and the ejecta.

A number of magnetohydrodynamics simulations have shown that the effective value of α_{vis} becomes $O(0.01)$ for disks rotating in the vicinity of central remnants (e.g., Kiuchi et al. 2018; Fernández et al. 2019). In addition, in our previous work (Fujibayashi et al. 2018), we found that (if $\alpha_{vis} \leqslant 0.04$) features of the postmerger ejecta do not depend strongly on the viscous parameter except for the mass-ejection timescale, which is approximately proportional to α_{vis}^{-1}. Therefore, we set $\alpha_{vis} = 0.04$ for our fiducial models in this work. For the DD2-125 model, we also perform a simulation with a very high viscosity $\alpha_{vis} = 0.10$ (DD2-125M-h) to explore the dependence of the result on the viscosity strength (i.e., the timescale of the viscous evolution of the system).

2.7. Particle Trace Method

The evolutions of our grid-based hydrodynamical quantities should be converted into Lagrangian particle motions for the nucleosynthesis calculations (Section 4). For this purpose, we adopt a tracer particle method (Wanajo et al. 2014). As initial positions of the tracer particles, we select 128 points with polar angles in the range of $\theta = 0$–$\pi/2$ on the arc with the radius of $r_{esc} = 8000$ km. We repeat the same procedure every $\Delta t_{set} = 0.05$ s to set tracer particles. The mass of each particle is set based on the radial mass flux of its initial position as

$$\Delta m = r_{esc}^2 \Delta\Omega \rho_* v^r \Delta t_{set}, \tag{13}$$

where $\Delta\Omega$ is the solid angle element, $\rho_* = W^{-3}\alpha u^t \rho$, and $v^r = dr/dt$. It depends on the polar angle and the time at which the particle is set initially. In this manner, the total mass of the particles, M_{traj}, is compatible with the ejecta mass defined in Section 3.3. We then evolve them backward in time. The numerical method of tracing particles is basically the same as that in Nishimura et al. (2015) except for the difference in the coordinate system employed. The time integration is based on the predictor-corrector method with second-order accuracy. We use bilinear interpolation to convert grid-based hydrodynamical quantities into those of the tracer particles. The particle position $(x^{(n)}, z^{(n)})$ at time $t^{(n)}$ is obtained from

$$x^{(n)} = x^{(n+1)} + v^{x*}\Delta t, \tag{14}$$

$$z^{(n)} = z^{(n+1)} + v^{z*}\Delta t, \tag{15}$$

where v^{x*} and v^{z*} denote the modified velocity components of the particle estimated by the predictor-corrector method and $\Delta t = t^{(n)} - t^{(n+1)}$ (<0).

3. Simulation Results

3.1. Dynamics of the System

Although the qualitative evolution process of the postmerger remnant composed of a massive NS and an accretion disk was already described in our previous paper (Fujibayashi et al. 2018), we briefly summarize it again in this subsection. Figure 1 shows snapshots of the rest-mass density, electron fraction, temperature, and entropy per baryon for model DD2-125M. The top-left panel of Figure 1 shows the initial profile of the simulation. There is a dense disk extending to ~ 100 km around the massive NS. The disk has high density ($\rho \sim 10^{12}$ g cm^{-3}), high temperature ($k_B T \sim 10$ MeV), and low electron fraction ($Y_e \lesssim 0.1$). The material of low electron fraction is located in the region with the density of $\sim 10^6$ g cm^{-3} around the equatorial plane. This material was expelled during the dynamical merger phase without experiencing significant positron capture by neutrons because of its low temperature and resulting in poor electron–positron pair creation. Part of this material is the dynamical ejecta, and the rest is still mechanically bound.

The massive NS formed as a remnant after the binary NS merger is differentially rotating and it is first evolved by the viscous effect (before the disk is evolved). The timescale is estimated as

$$\frac{R_{eq}^2}{\nu} \approx 5 \text{ ms} \left(\frac{\alpha_{vis}}{0.04}\right)^{-1} \left(\frac{c_s}{c/3}\right)^{-1}$$
$$\times \left(\frac{R_{eq}}{15 \text{ km}}\right)^2 \left(\frac{H_{tur}}{10 \text{ km}}\right)^{-1}, \tag{16}$$

where R_{eq} is the equatorial radius of the NS, and we use Equation (9) for the viscous coefficient ν. In this timescale, the rotational profile of the massive NS is modified due to the viscous angular momentum transport. This produces the early viscosity-driven ejecta, powered by the kinetic energy of differential rotation of the NS, in particular in its outer region.[9]

The range of the electron fractions of this component is approximately the same as that of dynamical ejecta (see Section 3.3.3). The amount of this component depends on the viscous parameter α_{vis} as found in Section 3.4.

In the polar direction, the high-entropy material is ejected mainly due to the heating by neutrinos emitted from the remnant (panels for $t > 0$ s of Figure 1). This polar mass ejection is efficient in particular for $t \lesssim 0.1$ s during which time neutrinos are copiously emitted from the disk (see Section 3.2.3). After that, this mass ejection becomes weak with the decrease of the neutrino luminosity. However, the polar mass ejection still continues throughout our simulation time, because the massive NS is present and continuously emits neutrinos (see Figure 3).

The disk gradually expands due to the outward viscous angular momentum transport and viscous heating, while the temperature of the disk decreases because of the expansion and

---

[9] In our previous work (Fujibayashi et al. 2018), we described that this mass ejection was powered by the rotational kinetic energy of the entire region in the NS. However, as found in Appendix B, the inner region of the NS contributes only slightly to the mass ejection, and the viscous effect on the surface of the NS, which has the largest angular velocity, drives the mass ejection. We also find that the mass of this ejecta component depends weakly on the magnitude of ζ. This indicates that this early component is partially due to the transitional effect in the timescale of ζ^{-1}, in which the viscous tensor $\tau^0_{\alpha\beta}$ approaches $\sigma_{\alpha\beta}$.
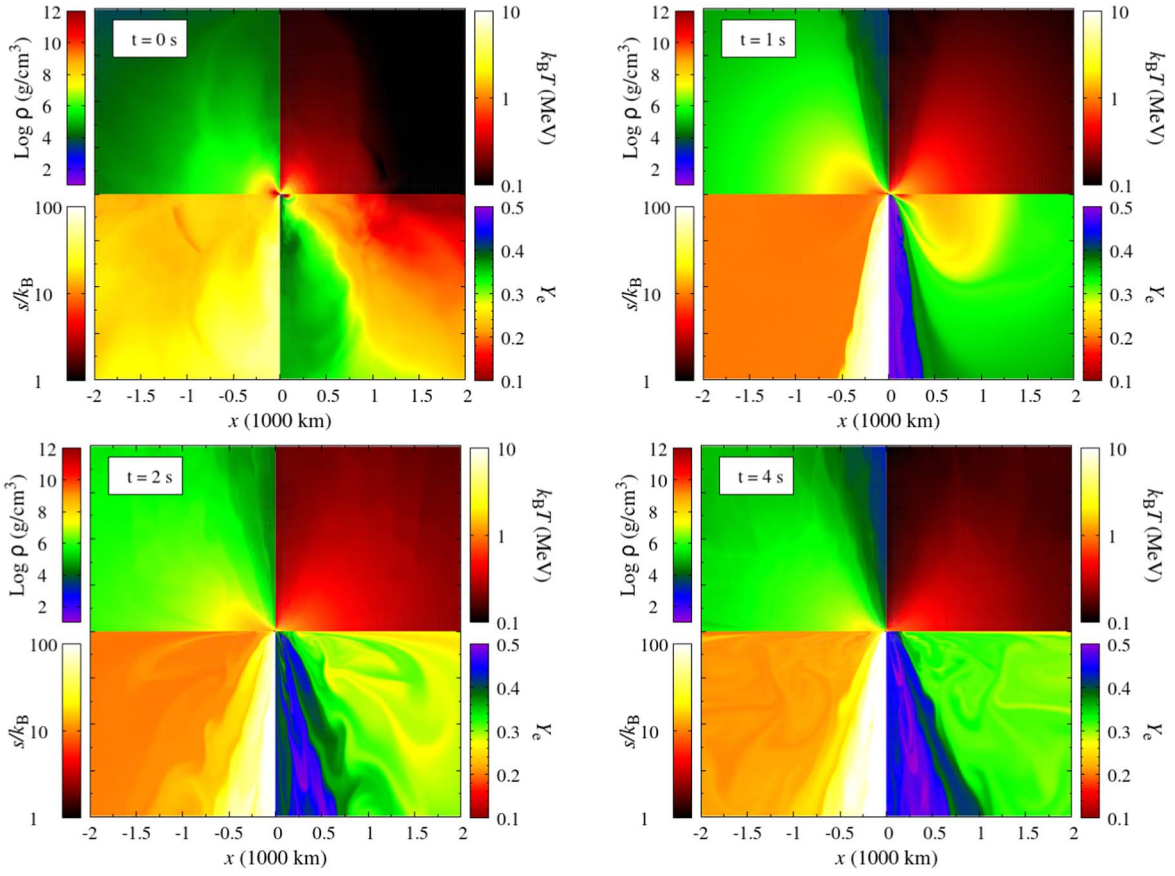
Figure 1. Snapshots for model DD2-125M at $t = 0$, 1, 2, and 4 s. Each panel with the color bars displays the profiles of the rest-mass density (top left), temperature (top right), entropy (bottom left), and electron fraction (bottom right).

neutrino cooling. When the neutrino cooling rate becomes lower than the viscous heating rate, the disk material begins to be ejected because most of the viscous heating is used for the disk expansion. This late-time viscosity-driven ejecta consists mainly of the material with $Y_e = 0.3$–0.35 and $s/k_B \approx 10$ (panels for $t > 0$ s of Figure 1; see also Section 3.3.3). The dynamics of the system among the explored models is quite similar to each other, although the properties of the ejecta depend quantitatively on the EOS, mass of the massive NS, and the magnitude of α_{vis}.

3.2. Remnant Massive NS and Disk

3.2.1. Radius of the NS Surface

In this section, we present the time evolution of quantities related to the massive NS and the disk surrounding it for each model. First, we describe how we distinguish the disk from the outer part of the massive NS.

It is not trivial to define the boundary that divides these two components, because the material of the massive NS is continuously connected to the disk (i.e., the density varies continuously). We use the angular velocity profile to define the NS and disk components, respectively. The top panel of Figure 2 shows the angular velocity profile along the equatorial plane at selected time slices for DD2-125M. At $t = 0$, the system including the high-density region of the remnant ($x \lesssim 15$ km) is entirely in a differentially rotating state. The angular velocity is small in the central region, peaks at ≈ 10 km, and then decreases with the radius. This is the typical rotational

profile of a merger remnant (e.g., Shibata et al. 2005). Within a few milliseconds after the simulation begins, the rotational profile of this region changes to become rigid due to a viscous angular momentum transport process, the timescale of which is estimated by Equation (16). This is clearly illustrated in the middle panel of Figure 2, which shows the logarithmic derivative of the angular velocity with respect to the cylindrical radius, i.e., $d \ln \Omega / d \ln x$. For $t > 0.01$ s, the innermost region (with $x \lesssim 15$ km) settles into a rigidly rotating state, i.e., $d \ln \Omega / d \ln x \approx 0$. On the other hand, in the outer region with $x \gtrsim 15$ km, its value gradually approaches the Keplerian value of -1.5, which is the expected feature of the disk. We define the NS radius, R_{NS}, as the innermost cylindrical radius that satisfies $d \ln \Omega / d \ln x = -0.1$ on the equatorial plane. Although the value is defined along the equatorial direction, we employ this in all polar angle directions to define the NS region (i.e., the NS region is assumed to be spherical).

We note that defining the NS surface in terms of density is nontrivial particularly in an early stage of the evolution ($t \lesssim 0.3$ s), wherein the density gradient at the NS surface is not sufficiently large. However, for $t \gtrsim 0.3$ s, the density can also be used to separate the two regions because the density gap between those regions becomes very large.

The bottom panel of Figure 2 shows the angular velocity evolution for model DD2-135M-v14, in which the viscosity is switched off for the region with the rest-mass density above 10^{14} g cm^{-3} to clarify that the inner region of the NS does not have a significant impact on the early viscosity-driven ejecta (for this model, $d \ln \Omega / dx$ is positive or close to zero inside the
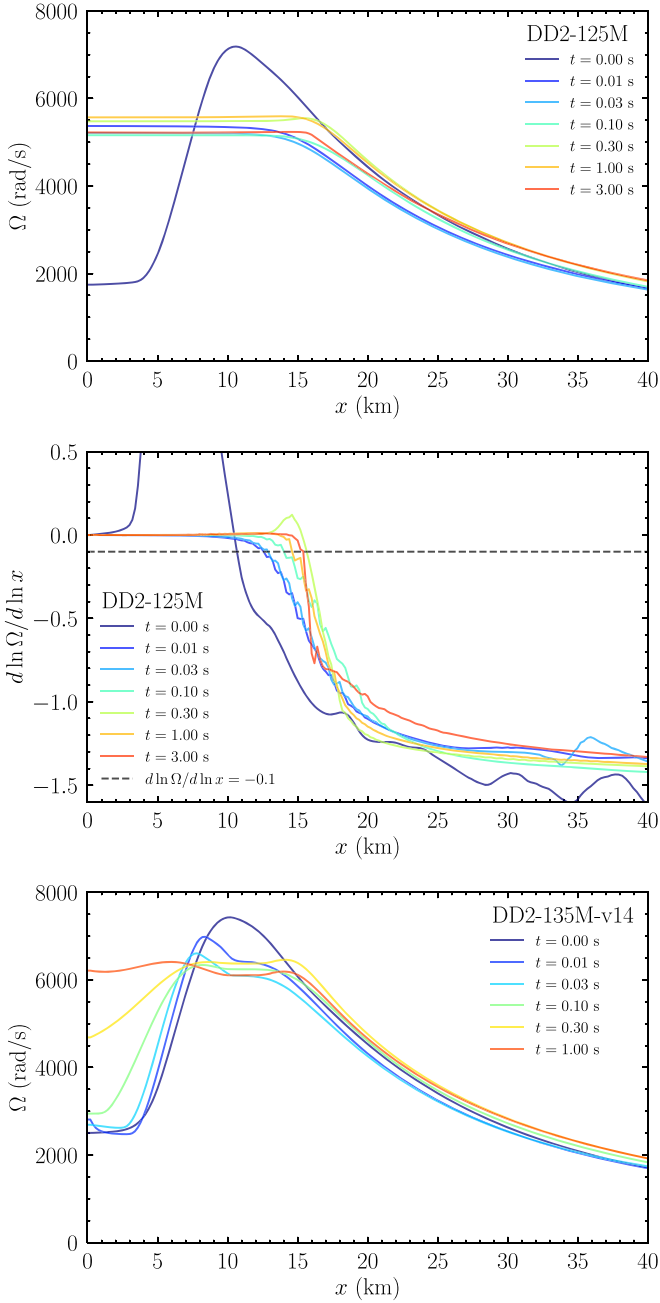
Figure 2. Angular velocity (top) and its logarithmic derivative with respect to the cylindrical radius (middle) along the equatorial plane for model DD2-125M. The bottom panel shows the angular velocity evolution for model DD2-135M-v14.

NS). In this model, $d\ln\Omega/d\ln x$ also steeply decreases for $x \gtrsim 15$ km and thus we can define the NS surface in the method mentioned above. On the other hand, the viscous angular momentum transport does not occur inside a radius of ≈ 10 km, in which the rest-mass density is higher than 10^{14} g cm^{-3}.

We note that, as illustrated in Appendix B, the properties of the early viscosity-driven ejecta for this model are not significantly different from those of DD2-135M. This shows that the early ejecta component is driven by releasing the rotational kinetic energy near the NS surface (not the main body of the NS). We find that the slow increase of the angular

velocity for $t \gtrsim 0.1$ s in this model is due to the convective motion inside the stellar body (see Appendix B).

3.2.2. Diagnostics

With the radius of the NS surface determined above, we define the baryon rest mass, angular momentum, and neutrino luminosity of the NS as

$$M_{\rm NS} = \int_{r\leqslant R_{\rm NS}} d^3x \, \rho_*, \tag{17}$$

$$J_{\rm NS} = \int_{r\leqslant R_{\rm NS}} d^3x \, \rho_* h u_\phi, \tag{18}$$

$$L_{\nu,\rm NS} = \int_{r\leqslant R_{\rm NS}} d^3x \, \alpha W^{-3} Q_{(\rm leak)t}, \tag{19}$$

where $Q_{(\rm leak)t}$ is the time component of the leakage rate (see Section 2.2). Here we multiply the lapse function α to take the gravitational redshift into account for the neutrino luminosity, and thus, this luminosity corresponds to the value observed at infinity. The quantities for the disk ($M_{\rm disk}$, $J_{\rm disk}$, and $L_{\nu,\rm disk}$) are also defined by integrating the same quantities in the region of $r > R_{\rm NS}$. We also define the average electron fraction, average entropy, and total viscous heating rate of the disk by

$$Y_{\rm e,disk} = \frac{1}{M_{\rm disk}} \int_{r>R_{\rm NS}} d^3x \, \rho_* Y_{\rm e}, \tag{20}$$

$$s_{\rm disk} = \frac{1}{M_{\rm disk}} \int_{r>R_{\rm NS}} d^3x \, \rho_* s, \tag{21}$$

$$L_{\rm vis,disk} = \int_{r>R_{\rm NS}} d^3x \, \alpha W^{-3} \frac{1}{2} \rho h \nu \tau^{0\alpha\beta} \tau^0{}_{\alpha\beta} u_t, \tag{22}$$

where $(1/2)\rho h \nu \tau^{0\alpha\beta}\tau^0{}_{\alpha\beta}$ is the viscous heating rate in the fluid rest frame (see Section 2.6 in Fujibayashi et al. 2018).

3.2.3. Properties of the NS

The top and middle panels of Figure 3 show the baryon mass and angular momentum of the remnant massive NSs ($M_{\rm NS}$, $J_{\rm NS}$) for models DD2-125M, SFHo-125H, and DD2-135M. $M_{\rm NS}$ and $J_{\rm NS}$ increase with time in an early stage of its evolution, $t \lesssim 1$ s, in response to mass accretion. This mass accretion is caused primarily by the cooling of the disk material: the material located near the NS surface does not have Keplerian angular momentum and is sustained predominantly by the thermal pressure (see Figure 2). Through the neutrino cooling, the thermal pressure decreases and then the material falls onto the NS. The increase of the baryon mass is smaller for the SFHo case than for the DD2 cases simply due to the smaller disk mass for the SFHo case (see Table 3). For $t \gtrsim 0.5$ s, the total angular momentum of the NS begins to decrease, while the increase of the NS mass saturates. This is a consequence of the fact that neutrinos emitted from the rotating NS carry its angular momentum away (see Appendix A). The angular momentum loss rate is $\sim 10^{48}$ erg s s^{-1}, which is consistent with an analytic estimation presented in Appendix A.

The bottom panel of Figure 3 shows the neutrino luminosity of the massive NS and the disk for each model. The luminosity of the NS is $\sim (5–7) \times 10^{52}$ erg s^{-1} for $t \lesssim 0.1$ s and gradually decreases for $t > 0.1$ s. The slight increase of the luminosity for $t \gtrsim 0.5$ s is partly due to the finite grid resolution (see Appendix B). The neutrino luminosity of the disk is
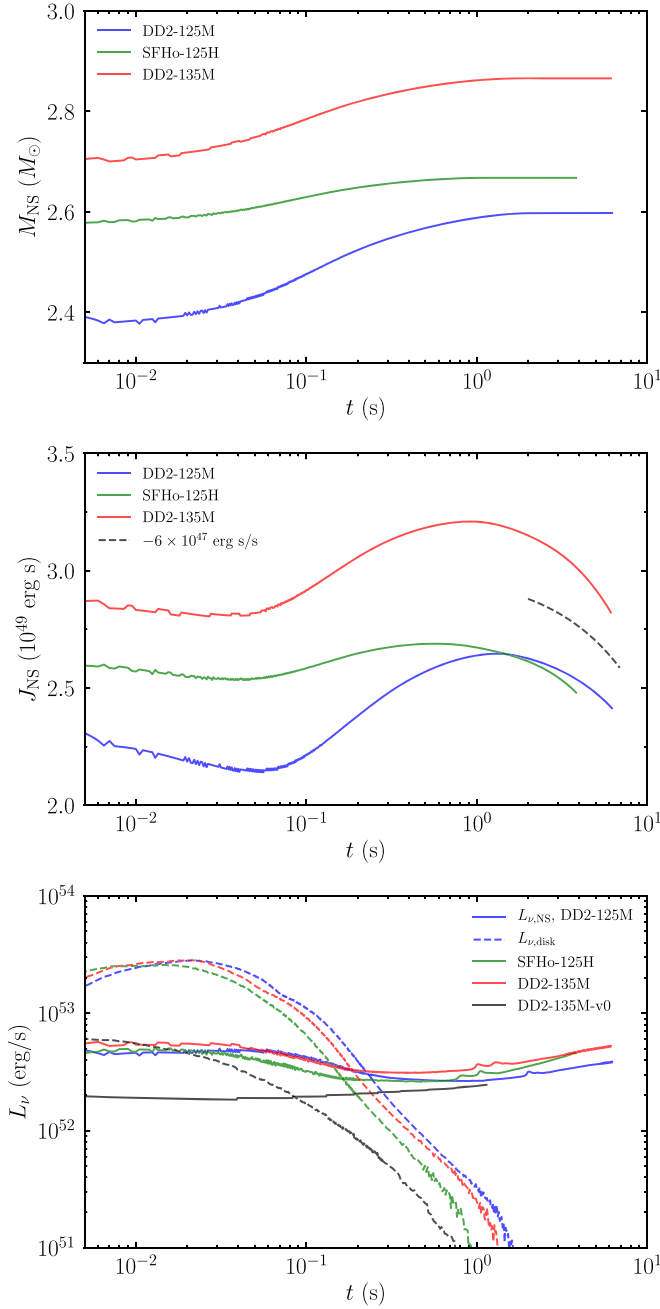
Figure 3. Baryon mass (top), angular momentum (middle), and total neutrino luminosity (bottom) of the NSs for models DD2-125M (blue), SFHo-125H (green), and DD2-135M (red). The dashed curve in the middle panel corresponds to the case of the constant angular momentum loss rate of 6×10^{47} erg s s^{-1} (see Appendix A). In the bottom panel, the neutrino luminosity of the disks is also plotted by the dashed curves and that for model DD2-135M-v0 is also shown.

$(1-3) \times 10^{53}$ erg s^{-1} for $t \lesssim 0.1$ s for each model, which is several times higher than that of the NS. The high luminosity is sustained for $t \lesssim 0.1$ s by the viscous heating in the disk. However, as the temperature of the disk decreases due to the neutrino cooling and viscous expansion, the luminosity decreases for $t \gtrsim 0.1$ s. By comparing models DD2-135M and DD2-135M-v0, we find that the viscous effect enhances the neutrino luminosity of the NS and disk by a factor of 3–5 for $t \lesssim 0.1$ s (for our choice of the viscous parameter, $\alpha_{\mathrm{vis}} = 0.04$). This enhancement of the neutrino luminosity

results in the larger amount of the neutrino-driven ejecta (see Section 3.3.2).

3.2.4. Properties of the Disk

The quantities relevant to the disks for models DD2-125M, SFHo-125H, and DD2-135M are shown in Figure 4. Note that this "disk" component includes unbound material (see the definition in Section 3.2.2). The baryon mass and angular momentum of the disk (M_{disk} and J_{disk}) rapidly drop during an early time of $t \lesssim 1$ s due to the mass accretion onto the NS caused by the neutrino cooling (see Section 3.2.3). The timescale of this accretion (i.e., the neutrino cooling timescale) is estimated by

$$\frac{M_{\mathrm{g,NS}} M_{\mathrm{disk}}}{R_{\mathrm{NS}} L_{\nu,\mathrm{disk}}} \approx 0.64 \text{ s}$$
$$\times \left(\frac{M_{\mathrm{g,NS}}}{2.5 M_\odot}\right)\left(\frac{M_{\mathrm{disk}}}{0.1 M_\odot}\right)\left(\frac{R_{\mathrm{NS}}}{10 \text{ km}}\right)^{-1}\left(\frac{L_{\nu,\mathrm{disk}}}{10^{53} \text{ erg s}^{-1}}\right)^{-1}, \quad (23)$$

where $M_{\mathrm{g,NS}}$ is the gravitational mass of the NS. The numerical result is consistent with this timescale.

The baryon mass and angular momentum of the disk for the SFHo case are smaller than those for the DD2 cases because of the smaller tidal effect on the merging NSs for the former. The disk mass is slightly larger for model DD2-125M than for DD2-135M, because the former has a smaller compactness and thus the self-gravity of the central massive NS is weaker. We note that the disk component has a nonnegligible fraction of the angular momentum of the remnant. The fraction of the disk angular momentum is 25%–30% of the total angular momentum of the remnant depending weakly on the EOS and the total mass of the system. Thus, only less than 75% of the total angular momentum of binary NSs at merger goes into the remnant massive NSs.

The disk mass is often defined by a certain density criterion (e.g., Shibata et al. 2017a; Radice et al. 2018). In the top-left panel of Figure 4, we also show the mass of the material with $\rho < 10^{12}$ g cm^{-3}, which agrees approximately with the mass using our criterion, $r > R_{\mathrm{NS}}$, at late times $t \gtrsim 0.1$ s.

We define the average radius of the disk R_{disk} by

$$R_{\mathrm{disk}} = \frac{1}{M_{\mathrm{g,NS}}} \frac{J_{\mathrm{disk}}^2}{M_{\mathrm{disk}}^2}, \quad (24)$$

where we assumed that J_{disk} can be approximated by $M_{\mathrm{disk}} \sqrt{M_{\mathrm{g,NS}} R_{\mathrm{disk}}}$, and for simplicity, we use the Arnowitt–Deser–Misner mass (ADM mass; Arnowitt et al. 1960) obtained initially in the simulation as the gravitational mass of the NS. We note that R_{disk} depends only on the average specific angular momentum, $J_{\mathrm{disk}}/M_{\mathrm{disk}}$, and does not change by the heating or cooling of the disk. Moreover, this is a good indicator of the disk radius only for the case where the disk has Keplerian motion and does not appropriately indicate the disk radius when the material in the disk starts to be ejected from the system.

The middle-left panel of Figure 4 shows that R_{disk} gradually increases, indicating that the average specific angular momentum of the disk increases. For the earlier phase $t \lesssim 1$ s, this occurs due to the accretion of the disk material with small specific angular momentum onto the NS due to the neutrino cooling. After the disk mass saturates for $t \gtrsim 1$ s, it is due to the
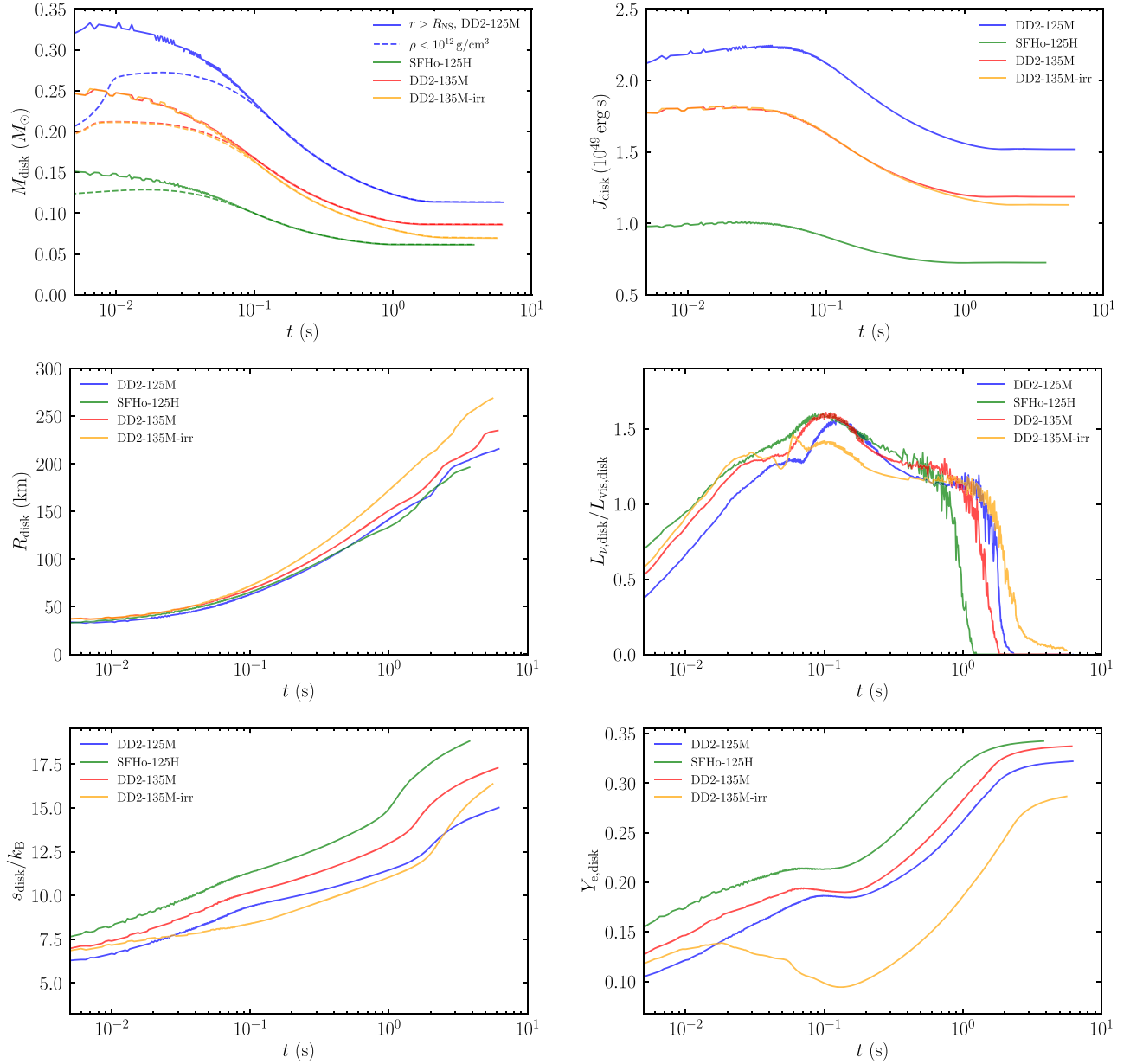
Figure 4. Mass (top left), angular momentum (top right), average radius (middle left), the ratio of neutrino luminosity to viscous heating rate (middle right), average entropy (bottom left), and electron fraction (bottom right) of the disks for models DD2-125M, SFHo-125H, DD2-135M, and DD2-135M-irr. In the top-left panel, the mass in the region with $\rho < 10^{12}$ g cm^{-3} is also plotted by the dashed curve for each model. In the top two panels, the saturated values indicate the total ejecta mass ($M_{\rm ej,tot}$) and angular momentum. We note that the disk material here implies the material located outside the massive NS and contains the unbound component.

viscous angular momentum transport from the outer envelope of the NS to the disk.

In the middle-right panel of Figure 4, we plot the ratios of the total (net) neutrino luminosity of the disk, $L_{\nu,\rm disk}$, which also includes the heating by neutrino interaction, to the viscous heating rate in the disk, $L_{\rm vis,disk}$, for each model. The ratio increases with time for $t \lesssim 0.1$ s because the optical depth of the disk, which is $\sim$10–100 at the beginning of the simulation, decreases due to the accretion and expansion of the disk. It peaks at $t \sim 0.1$ s, when the optical depth of the disk decreases to $\sim$1 and neutrinos can carry away the thermal energy generated by the viscous heating and stored in the opaque disk. Then, the ratio decreases to $\sim$1 for 0.1 s $\lesssim t \lesssim 1$ s, when the disk is optically thin and the viscously generated thermal energy can be emitted immediately. For $t \lesssim 1$ s, the ratio is close to or larger than unity, indicating that viscous heating

does not contribute substantially to the disk expansion. However, after the accretion timescale of the disk ($\sim$1 s; see Equation (23)), the neutrino emission and the disk accretion become weaker. Then, for $t \gtrsim 1$ s, this ratio drops steeply. This implies that the neutrino cooling is no longer efficient and most of the viscous heating is used for the disk expansion. We note that $t \sim 1$ s also corresponds to the time at which the weak-interaction timescale becomes longer than the timescale of the viscous expansion of the disk (i.e., the weak interaction freezes out; see Section 3.3).

In Figure 4, we also plot the evolution of the average entropy (bottom left) and electron fraction (bottom right) of the disk, which increase gradually with time. The increase of the entropy is due to the viscous and neutrino heating. The electron fraction of the disk is determined by an equilibrium condition of electron/positron capture. Its equilibrium value becomes

higher during the disk expansion because the electron degeneracy becomes weaker (the neutrino irradiation plays a minor role for the increase of the electron fraction; see Section 3.3). Its increase stagnates at $t \sim 0.1$ s because of the feedback effect of the efficient neutrino emission (Chen & Beloborodov 2007; Kawanaka & Mineshige 2007): as the middle-right panel of Figure 4 shows, the efficiency of the neutrino emission at $t \sim 0.1$ s is quite high. In such a situation, the increase of the specific entropy through viscous heating is suppressed (bottom-left panel of Figure 4). As a result, the electron degeneracy is kept strong, suppressing the increase of Y_e (bottom-right panel of Figure 4). Due to the neutrino irradiation, the value of the electron fraction at $t \sim 0.1$ s in our models (~ 0.2) is higher by ~ 0.1 than that found in the context of the disk around a BH (Siegel & Metzger 2018). In the absence of the neutrino irradiation, the electron fraction becomes lower (see Section 3.2.5). After the neutrino cooling becomes inefficient, the entropy increases continuously, while the electron fraction saturates after the gradual increase until $t \sim 1$ s, because the timescale of electron/positron capture in the disk becomes longer than the viscous evolution timescale due to the decrease of the temperature (see Section 3.3). The final average value of Y_e is 0.30–0.35.

3.2.5. Effect of the Neutrino Irradiation on the Properties of the Disk

Figure 4 also shows the quantities for model DD2-135M-irr, in which the neutrino irradiation is switched off. Here, we explore the effect of neutrino irradiation on the quantities of the disk by comparing models DD2-135M and DD2-135M-irr. For model DD2-135M-irr, the neutrino cooling of the inner part of the disk, which has a smaller specific angular momentum than the outer part, is more efficient than that for model DD2-135M because of the absence of neutrino irradiation. As a result, the average specific angular momentum of the disk (J_{disk}/M_{disk}), and thus the average disk radius (R_{disk}) increase more quickly than those for model DD2-135M.

In addition, the average electron fraction of the disk is lower by 0.05–0.1 than that for model DD2-135M throughout the evolution because of the absence of neutrino irradiation, which usually increases the electron fraction. At $t \sim 0.1$ s, due to the feedback effect, the average electron fraction of the disk is maintained to be ~ 0.1, which is consistent with that found in the disk around a BH without neutrino irradiation (Chen & Beloborodov 2007; Kawanaka & Mineshige 2007; Siegel & Metzger 2018). Because the electron fraction of the disk becomes lower, the electron fraction of the late-time viscosity-driven ejecta also becomes lower (see Section 3.3.2).

3.3. Ejecta

3.3.1. Diagnostics

In this subsection, we describe the properties of the ejecta. First of all, we summarize the method to calculate the ejecta quantities. We define the mass of the ejecta that escaped from a sphere, $M_{ej,esc}$, by integrating the unbound material outflowing through the surface of a radius r_{esc},

$$M_{ej,esc} = \int^t dt \frac{dM_{ej,esc}}{dt}, \qquad (25)$$

where the mass-ejection rate is defined by

$$\frac{dM_{ej,esc}}{dt} = \int dS_k v^k \rho_* H(-hu_t - h_{min}), \qquad (26)$$

with the area element on the sphere dS_k and the Heaviside function H. Hereafter, as in Section 2.7, r_{esc} is set to 8000 km, at which the temperature of the material is sufficiently low and the recombination of free nucleons has already occurred. Thus, Equation (12) can be a suitable condition for the material being unbound.

We also define the rate of the total energy (sum of the rest mass, and internal and kinetic energy) of the ejecta passing through the radius r_{esc} as

$$\frac{dE_{ej,esc}}{dt} = \int dS_k v^k \rho_* \hat{e} H(-hu_t - h_{min}), \qquad (27)$$

where $\hat{e} = h\alpha u^t - P/(\rho \alpha u^t)$ and the total energy of the ejecta is calculated by

$$E_{ej,esc} = \int^t dt \frac{dE_{ej,esc}}{dt}. \qquad (28)$$

This quantity is decomposed in the region far from the source of the gravity into

$$E_{ej,esc} \approx M_{ej,esc} + T_{kin} + U + \frac{M_{ej,esc}M_{g,NS}}{r_{esc}}, \qquad (29)$$

where T_{kin} and U are the kinetic and internal energies of the ejecta at a sufficiently distant region, and the last term approximately denotes the contribution from the gravitational binding energy. For the gravitational mass of the NS, we again use the ADM mass with the value obtained at the beginning of the simulation. From these expressions, we define the average ejecta velocity by

$$\langle V_{ej} \rangle = \sqrt{2\left(\frac{E_{ej,esc}}{M_{ej,esc}} - 1 - \frac{M_{g,NS}}{r_{esc}}\right)}, \qquad (30)$$

where we assumed that the internal energy of the ejecta is eventually transformed into its kinetic energy during its expansion, i.e., $T_{kin} + U = M_{ej,esc}\langle V_{ej} \rangle^2/2$ at infinity. Because there are several ejecta components having different velocities, we define the velocity of the material passing through the sphere at a given time by

$$V_{ej} = \sqrt{2\left(\left(\frac{dM_{ej,esc}}{dt}\right)^{-1} \frac{dE_{ej,esc}}{dt} - 1 - \frac{M_{g,NS}}{r_{esc}}\right)}, \qquad (31)$$

where we used a differential form of Equation (29) and assumed

$$\frac{d}{dt}(T_{kin} + U) = \frac{1}{2}\frac{dM_{ej,esc}}{dt}V_{ej}^2. \qquad (32)$$

With this definition, we can derive the velocity of the material ejected at different times.

There is still material satisfying Equation (12) inside the sphere with $r = r_{esc}$ at the end of the simulations. Thus, we
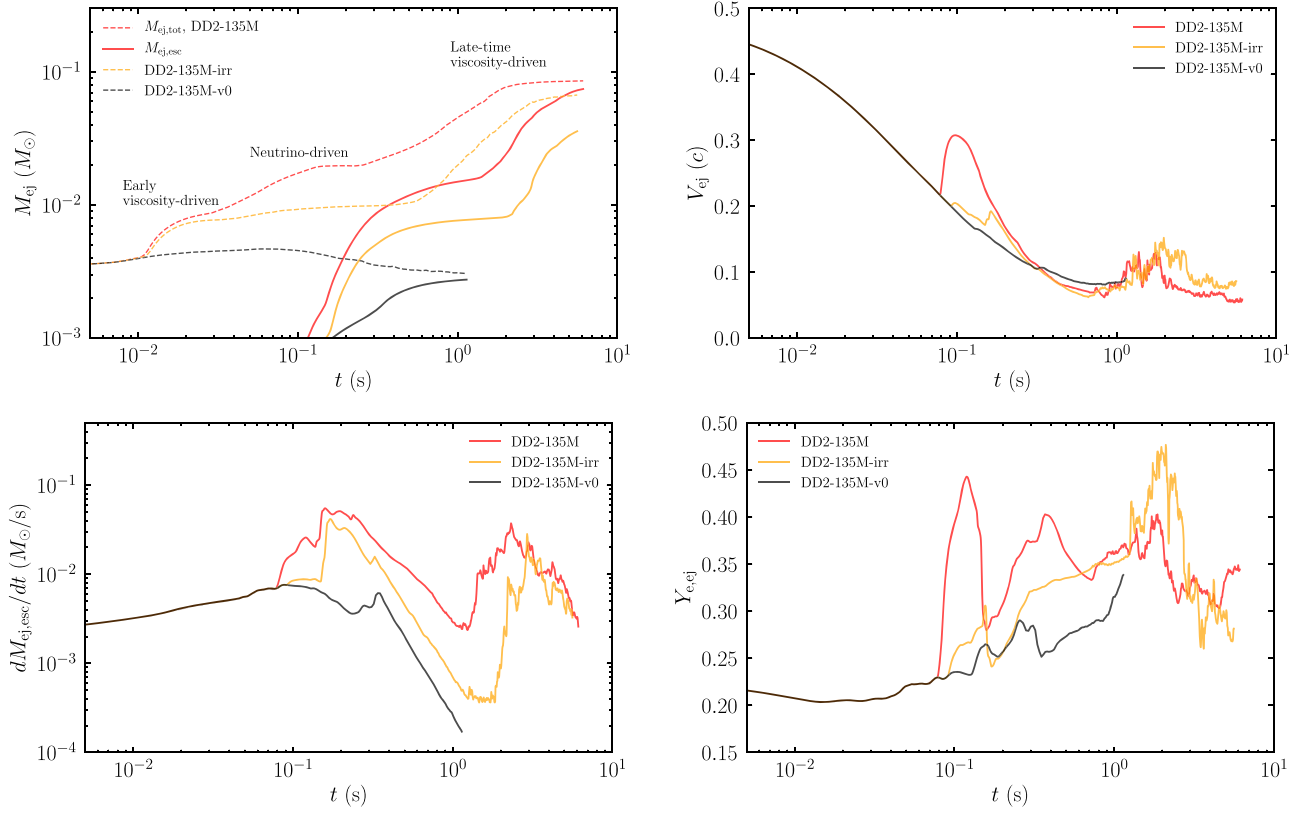
Figure 5. Ejecta masses ($M_{\rm ej,tot}$ and $M_{\rm ej,esc}$; top left), ejecta velocities ($V_{\rm ej}$; top right), mass-ejection rates ($dM_{\rm ej,esc}/dt$; bottom left), and average electron fraction ($Y_{\rm e,ej}$; bottom right) for models DD2-125M, DD2-135M-irr, and DD2-135M-v0. In the top-left panel, the solid and dashed curves show $M_{\rm ej,tot}$ and $M_{\rm ej,esc}$, respectively.

define the total mass by

$$M_{\rm ej,tot} = M_{\rm ej,esc}$$
$$+ \int_{500\,{\rm km} \leqslant r < r_{\rm esc}} d^3x \rho_* H(-hu_t - h_{\rm min}). \quad (33)$$

This value is interpreted approximately as the maximum mass that the merger remnant can eject. We define the mass-weighted average electron fraction of this material by

$$\langle Y_{\rm e,ej} \rangle = \frac{1}{M_{\rm ej,tot}} \left(\int^t dt \int dS_k v^k \rho_* Y_{\rm e} H(-hu_t - h_{\rm min}) \right.$$
$$\left. + \int_{500\,{\rm km} \leqslant r < r_{\rm esc}} d^3x \rho_* Y_{\rm e} H(-hu_t - h_{\rm min}) \right), \quad (34)$$

which includes both the ejecta that already escaped from and still stays inside the sphere of $r = r_{\rm esc}$. In order to derive the electron fraction of the different ejecta components, we also define the flux-weighted average electron fraction of the material passing through the sphere at a given time by

$$Y_{\rm e,ej} = \frac{1}{dM_{\rm ej,esc}/dt} \int dS_k v^k \rho_* Y_{\rm e} H(-hu_t - h_{\rm min}). \quad (35)$$

3.3.2. Contribution of Different Ejecta Components

In Figure 5, the ejecta mass (top left), mass-ejection rate (bottom left), ejecta velocity (top right), and average electron fraction (bottom left) for models DD2-135M, DD2-135M-irr, and DD2-135M-v0 are compared to explore the contribution of the effects of neutrino irradiation and viscosity. Here, we focus

on the models of the remnant of the merger with a large total gravitational mass of $2.7\,M_\odot$. The following discussion is also provided for models DD2-125M and SFHo-125M. At the very beginning of the simulation, unbound material of $M_{\rm ej,tot} \approx 0.004\,M_\odot$ was present, reflecting the merger process for this model. This amount is somewhat larger than that shown in Table 2 because of the difference in the definition of ejecta (see Sections 2.3 and 2.5). For the inviscid model DD2-135M-v0, $M_{\rm ej,tot}$ peaks at $t \sim 0.1$ s and then decreases, indicating that part of the ejecta was not actually the ejecta component, and it falls back to the central region. Its saturated value for $t \gtrsim 1$ s, $\approx 0.003 M_\odot$, is the actual mass of the ejecta. With the viscosity, on the other hand, a larger amount of material is ejected as described below.

For model DD2-135M, it is found that $M_{\rm ej,tot}$ increases at three different times, $t \sim 0.01$, ~ 0.1, and ~ 1 s (see the top right panel of Figure 5). The first increase of $M_{\rm ej,tot}$ at $t \sim 0.01$ s is also found for model DD2-135M-irr but absent for model DD2-135M-v0, and therefore, this increase is due to the viscous effect. This is the contribution of the early viscosity-driven ejecta. By comparing models DD2-135M and DD2-135M-v0, the contribution of this component for our choice of the viscous parameter ($\alpha_{\rm vis} = 0.04$) is found to be $\sim 0.01\,M_\odot$. The second increase at $t \sim 0.1$ s is absent for model DD2-135M-irr, and hence, we confirm that this ejecta is driven by neutrino irradiation. By comparing models DD2-135M and DD2-135M-irr, the contribution of this neutrino-driven component is found to be $\sim 0.01\,M_\odot$. The contribution of neutrino irradiation is fairly large compared to DD2-135M-v0 because of the large neutrino luminosity of the remnant due to the viscous heating (see Figure 3). The third one at $t \sim 1$ s, which
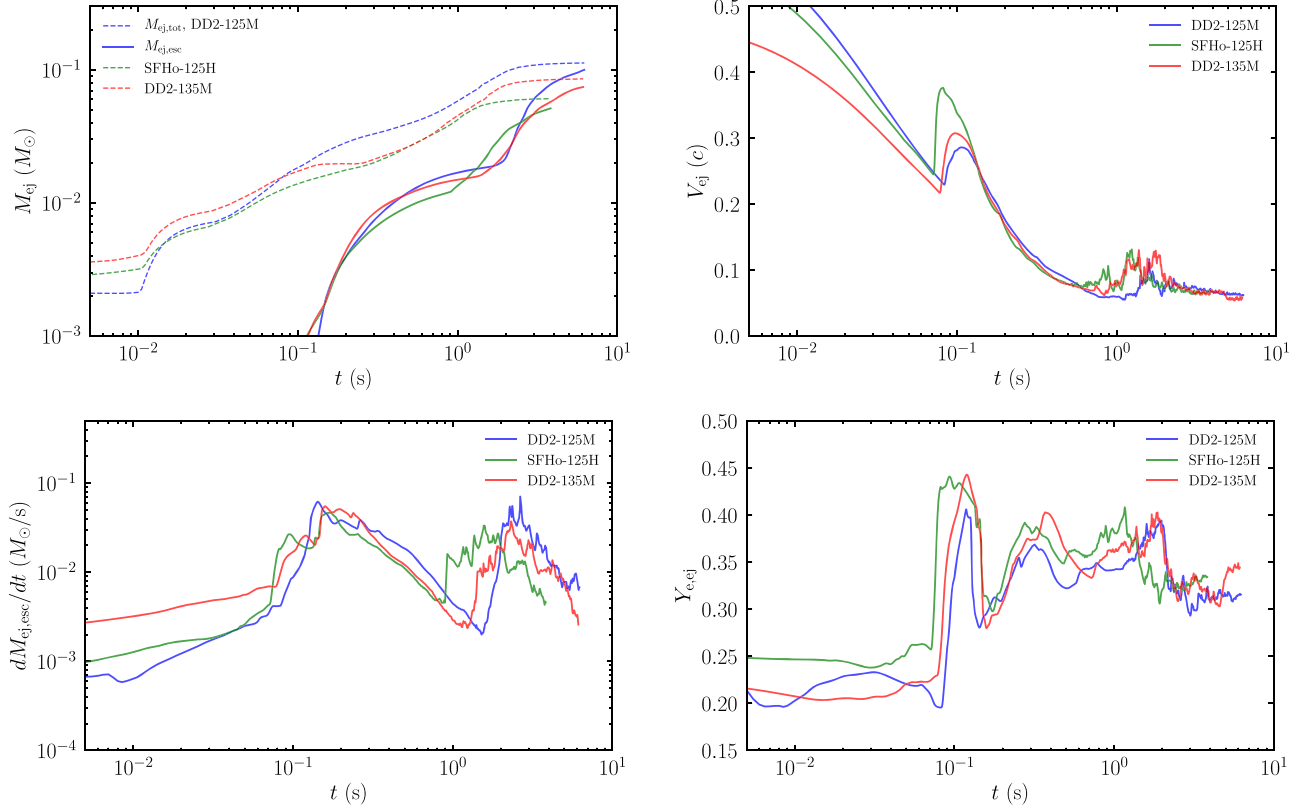
Figure 6. Same as Figure 5, but for models DD2-125M, SFHo-125H, and DD2-135M.

is found in both models DD2-135M and DD2-135M-irr, is the contribution of the late-time viscosity-driven ejecta.

In the bottom-left panel of Figure 5, only two (not three) distinct mass-ejection phases are found, one of which is found in an early phase of $t \lesssim 0.5$ s and the other is in a late phase of $t \gtrsim 1$ s. The former is composed of the dynamical, early viscosity-driven, and neutrino-driven components. The value of $dM_{\rm ej,esc}/dt$ for DD2-135M starts to deviate from that for model DD2-135M-irr at $t \approx 0.08$ s, indicating that the neutrino-driven component starts to contribute to $M_{\rm ej,esc}$ at this time. At $t \sim 0.1$ s, the properties of the ejecta are determined by both the dynamical and neutrino-driven ejecta, the former of which has a lower electron fraction of ≈ 0.2 and the latter a higher value of ≈ 0.55 (see Figure 8). $Y_{\rm e,ej}$ (the bottom-right panel of Figure 5) then has the average value of the two components, which is ≈ 0.40–0.45.

After that, the early viscosity-driven ejecta begins to contribute predominantly to the properties of the ejecta at $t \approx 0.2$ s, at which a peak in $dM_{\rm ej,esc}/dt$ is remarkable in particular for model DD2-135M-irr. This component has a low electron fraction of ≈ 0.25 as found for model DD2-135M-irr. $Y_{\rm e,ej}$ also decreases to ≈ 0.3 at this time for model DD2-135M as a result of the large contribution of the early viscosity-driven ejecta to $dM_{\rm ej,esc}/dt$.

In the top-right panel of Figure 5, a peak of $V_{\rm ej}$ at $t \sim 0.1$ s is found for model DD2-135M but absent for DD2-135M-irr, indicating that the neutrino-driven component has a velocity of $>0.3\,c$, which is larger than that of the dynamical and early viscosity-driven components at $t \approx 0.2$ s. This results in the simultaneous contribution of these ejecta components to

$dM_{\rm ej,esc}/dt$ at $t \sim 0.1$ s, although they are ejected at different times as found in the top-left panel of Figure 5.

Finally, the late-time viscosity-driven ejecta associated with the viscous effect in the disk sets in. $dM_{\rm ej,esc}/dt$ has a large value of $\gtrsim 0.01\,M_\odot$ s^{-1} for $t = 1$–3 s, and after that, it decreases with time. This component has a smaller velocity of $V_{\rm ej} \sim 0.05$–$0.10c$ and a range of the average electron fraction of $Y_{\rm e,ej} \approx 0.30$–$0.35$, reflecting the electron fraction of the disk ($Y_{\rm e,disk}$; see Figure 4).

For model DD2-135M, the mass-weighted average electron fraction over all ejecta components is $\langle Y_{\rm e,ej} \rangle \approx 0.34$ at the end of the simulation due to the domination of the late-time ejecta (see Table 3). By comparing models DD2-135M and DD2-135M-irr in Table 3, $\langle Y_{\rm e,ej} \rangle$ is lower by 0.05 in the absence of neutrino irradiation (reflected by the lower electron fraction of the disk; see Section 3.2.5).

It is worth mentioning that even in the absence of neutrino irradiation, the electron fraction of the ejecta increases to ≈ 0.3 due to the positron capture after the decrease of the electron degeneracy in the disk (see Section 3.3.4). This indicates that, even in the absence of a long-lived massive NS, the electron fraction of the ejecta would not be very low as pointed out in recent work for BH–disk systems (Fernández et al. 2020; Fujibayashi et al. 2020).

3.3.3. Ejecta Properties for Fiducial Models

Figure 6 compares the ejecta properties for models DD2-125M, SFHo-125H, and DD2-135M. The curves are qualitatively similar to each other, showing that there are three mass-ejection mechanisms as described in Section 3.3.2 irrespective of the adopted EOS and the total mass of the model. The

baryon mass of the unbound material for $t \lesssim 0.03$ s, composed of dynamical and early viscosity-driven ejecta, depends on models. The baryon mass of these early ejecta components correlates with the baryon mass of the dynamical ejecta (see Table 2). The amount of the subsequent neutrino-driven and late-time viscosity-driven ejecta, on the other hand, correlates with the disk mass (see the top-left panel of Figure 4). The value of $M_{\mathrm{ej,tot}}$ saturates at $t = 2$–3 s, and by comparing with the top-left panel of the Figure 4, the saturated values indicate that approximately 30% of the initial disk mass becomes the ejecta.

For all fiducial models, the average ejecta velocity is $\langle V_{\mathrm{ej}} \rangle \sim 0.1\ c$ (see Table 3), which is somewhat larger than that of the late-time ejecta (see the top-left panel of Figure 6) because of the large kinetic energy of the dynamical, early viscosity-driven, and neutrino-driven ejecta components.

Figure 7 shows the mass histograms of the electron fraction (top), entropy (middle), and expansion timescale (bottom; $t_{\mathrm{exp}} = r/v^r$) of the tracer particles at $T = 5$ GK for the fiducial models. The distributions for all models are quite similar and peak at $Y_{\mathrm{e}} \approx 0.3$, $s/k_{\mathrm{B}} \approx 10$, and $t_{\mathrm{exp}} \approx 0.1$ s. These peaks for each model are produced by the late-time viscosity-driven ejecta. In this figure, the histogram in the corresponding 3D simulations is also shown. This illustrates that the low electron fraction and short expansion timescale sides of the distributions are determined by the dynamical ejecta.[10]

The temporal Y_{e} distributions for the tracer particles that reach r_{esc} by a given time are shown in Figure 8 for models DD2-125M, SFHo-125H, and DD2-135M. At $t = 0.2$ s, there are two peaks at $Y_{\mathrm{e}} \sim 0.2$ and 0.55, which are determined by the dynamical plus early viscosity-driven ejecta and neutrino-driven ejecta, respectively. The subsequent change of the histograms clearly illustrates that the peak of Y_{e} in the final distribution is developed by the late-time viscosity-driven ejecta for $t > 1$ s.

The distributions of the ejecta in the s–Y_{e} plane are shown in Figure 9 for models DD2-125M, SFHo-125H, and DD2-135M. It is found that the distribution profiles depend very weakly on the EOSs and binary total mass. We also find a positive correlation between s and Y_{e}. The ejecta with $Y_{\mathrm{e}} \approx 0.3$ has an entropy of $s/k_{\mathrm{B}} \lesssim 10$, while the ejecta with higher values of Y_{e} has a higher entropy. The electron fraction for most of the material ejected toward the nonpolar direction is determined predominantly by the equilibrium between electron/positron capture (see Section 3.3.4), and the equilibrium value becomes higher for weaker electron degeneracy. Because the entropy negatively correlates with the electron degeneracy, the material with the higher entropy has the higher equilibrium value of the electron fraction. This results in the positive correlation between s and Y_{e}. In other words, the material experiencing the longer-time viscous heating has the higher electron fraction reflecting its higher entropy. By comparing the bottom two panels of Figure 9, it is found that the low-Y_{e} component is more abundant in the absence of neutrino irradiation.

In Figure 9, there is a component that has a low electron fraction of $Y_{\mathrm{e}} = 0.1$–0.2 and a moderate entropy of $s/k_{\mathrm{B}} \sim 50$. This component is a part of the dynamical ejecta, which is
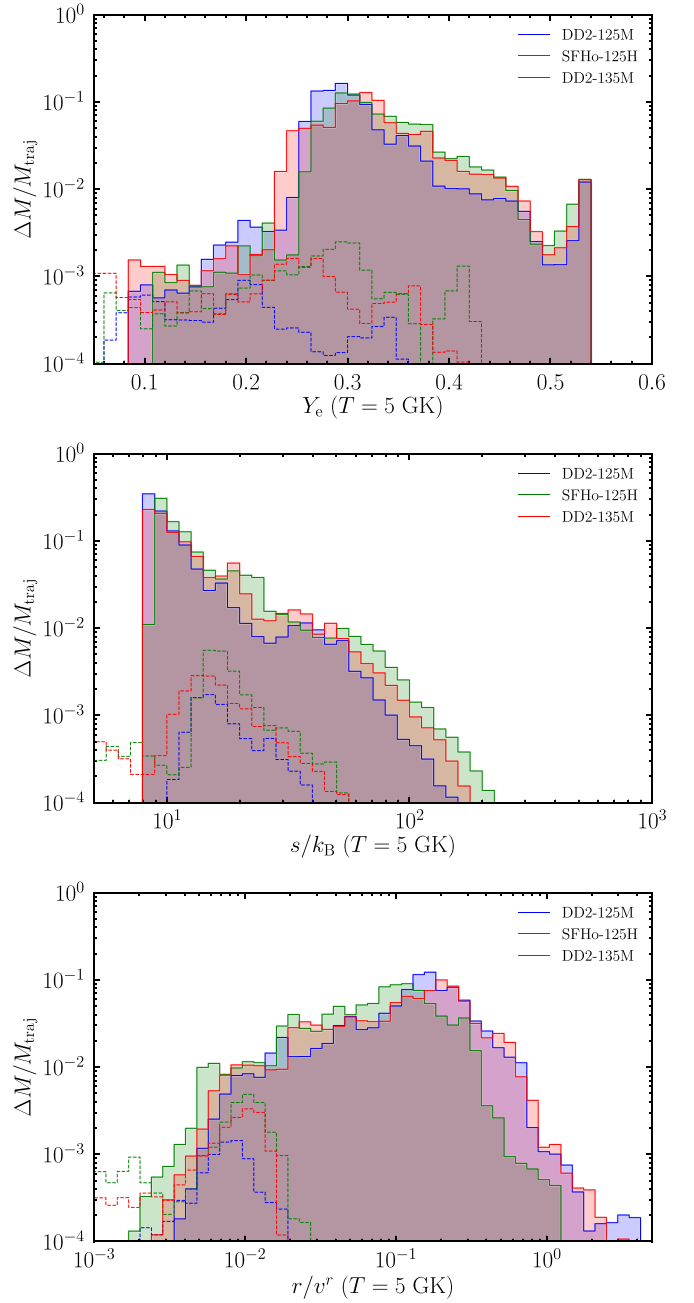

Figure 7. Mass histograms of the electron fraction (top), entropy (middle), and the expansion timescale (bottom) for tracer particles at $T = 5$ GK for models DD2-125M (blue), SFHo-125H (green), and DD2-135M (red). The dashed curves show the histograms obtained in the corresponding 3D models. Each histogram is normalized by the total mass of the tracer particles.

initially expelled by the tidal effect and then heated up by a shock formed in spiral arms. Because this component experiences shock heating in a distant region from the center, the increase in the temperature due to the shock is not enough for the weak interaction (positron capture) to work in a sufficiently short timescale. Thus, the electron fraction of this component remains low.

3.3.4. Processes that Determine the Electron Fraction of the Ejecta

The electron fraction of the material is approximately determined by the absorption of electron-type (anti)neutrinos

---

[10] In Figure 7, the lowest electron fraction, lowest entropy, and shortest expansion timescale ends found in 3D merger simulations are missing in 2D models. Due to the small mass fraction of such components, they disappear, because the 3D fluid profiles are averaged with respect to the azimuthal angle and mapped to the 2D initial conditions.

and the electron/positron capture on free nucleons. The time evolution of the electron fraction is described by

$$\dot{Y}_{\rm e} = \dot{Y}_{\rm e,\nu} + \dot{Y}_{\rm e,pc} - \dot{Y}_{\rm e,\bar{\nu}} - \dot{Y}_{\rm e,ec}, \qquad (36)$$

where $\dot{Y}_{\rm e,\nu}$, $\dot{Y}_{\rm e,\bar{\nu}}$, $\dot{Y}_{\rm e,ec}$, and $\dot{Y}_{\rm e,pc}$ are the change rates of the electron fraction due to the absorption (or capture) of electron neutrinos, electron antineutrinos, electrons, and positrons, respectively, on free nucleons. These reaction rates depend on the local density, temperature, electron fraction, and fluxes (and energies) of electron neutrinos and antineutrinos. In the top panel of Figure 10, the variations of the timescales of these reactions with decreasing temperature in tracer particles are shown together with their expansion timescales defined by $t_{\rm exp} = r/v^r$ with the coordinate radius r and radial velocity $v^r(=dr/dt)$. Here we define the timescale of the electron/positron capture by $t_{\rm cap} = \min(Y_{\rm e}/\dot{Y}_{\rm e,ec}, Y_{\rm e}/\dot{Y}_{\rm e,pc})$ and that of the neutrino absorption by $t_\nu = \min(Y_{\rm e}/\dot{Y}_{\rm e,\nu}, Y_{\rm e}/\dot{Y}_{\rm e,\bar{\nu}})$. It is found that until the timescales of weak-interaction processes become longer than the expansion timescale, the electron fraction of the tracer particle is determined mainly by the electron/positron capture (red) and subdominantly by the neutrino absorption (blue).

In the middle panel of Figure 10, the variation of the electron fraction with decreasing temperature in the tracer particles is shown together with its equilibrium values for neutrino and antineutrino absorption, $Y_{\rm e,\nu}$, and electron and positron captures, $Y_{\rm e,cap}$. These equilibrium values are determined by the equations $\dot{Y}_{\rm e,\nu} = \dot{Y}_{\rm e,\bar{\nu}}$ and $\dot{Y}_{\rm e,ec} = \dot{Y}_{\rm e,pc}$. Here, we assumed that the material is not optically thick to neutrinos. That is, in our analysis, we pay attention only to the temperature range in which the beta equilibrium is not established. This assumption is reasonable for low temperatures of $k_{\rm B}T \lesssim 3\,{\rm MeV}$. It is found that the electron fraction of the tracer particle is determined approximately by the equilibrium value for electron and positron captures for $k_{\rm B}T \sim 1\text{–}3\,{\rm MeV}$. We note that the electron fraction deviates from $Y_{\rm e,cap}$ for $k_{\rm B}T \gtrsim 3\,{\rm MeV}$ because the material is opaque to neutrinos and the electron fraction should be determined by the beta equilibrium; the electron fraction is determined not only by the electron/positron captures but also by electron (anti)neutrino absorption. By contrast, at $k_{\rm B}T \sim 1\,{\rm MeV}$, the electron fraction freezes out because the weak-interaction timescale becomes longer than the expansion timescale (see the top panel of Figure 10). This illustrates how the electron fraction is determined in the material ejected toward the nonpolar direction (see Figure 8). The effect of the neutrino absorption on the electron fraction is minor for most of the material ejected toward the nonpolar direction. On the other hand, for the material ejected toward the polar direction, the electron fraction is determined predominantly by the neutrino absorption, and it is higher than that of the ejecta toward the nonpolar direction (see Figure 1).

Because the equilibrium value of the electron fraction changes steeply in the temperature region of $k_{\rm B}T \approx 1\text{–}2\,{\rm MeV}$, at which the freeze out of weak interaction occurs, the electron fraction of the ejecta should be affected significantly by the expansion timescale. In the presence of strong viscous effect with $\alpha_{\rm vis} > 0.04$ or the other short-timescale mass-ejection processes (for example, the Lorentz force by aligned magnetic fields; see Section 3.5), the electron fraction of the ejecta would become lower (see Section 3.4).
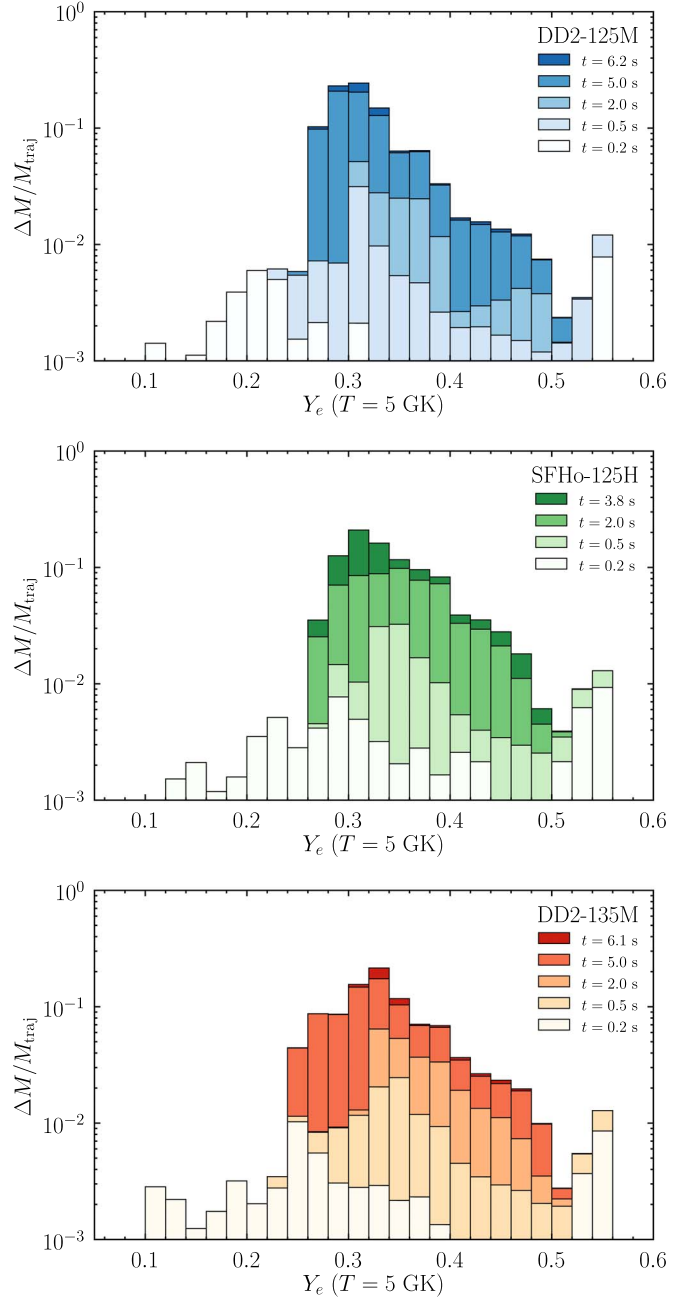

Figure 8. Temporal mass histograms of $Y_{\rm e}$ for the tracer particles that reach the radius $r_{\rm esc}$ by a given time for models DD2-125M (top), SFHo-125H (middle), and DD2-135M (bottom). Each histogram is normalized by the total mass of the tracer particles. Note that the range of the vertical axis for these panels differs from that of Figure 7.

In the bottom panel of Figure 10, the specific heating rates due to viscous dissipation and neutrino absorption are shown together with the specific cooling rate due to the neutrino emission. We note that the cooling rate shown in this figure is equal to the leakage rate in Equation (4), in which neutrino trapping is taken into account. The heating rate is suppressed in the optically thick region in our leakage-based neutrino radiation transfer method because part of the neutrino absorption is assumed to balance out the neutrino emission (see Fujibayashi et al. 2017 for a detailed description of our method). As a result, the heating rate for $k_{\rm B}T \gtrsim 2\,{\rm MeV}$ decreases with increasing temperature (i.e., high-density and
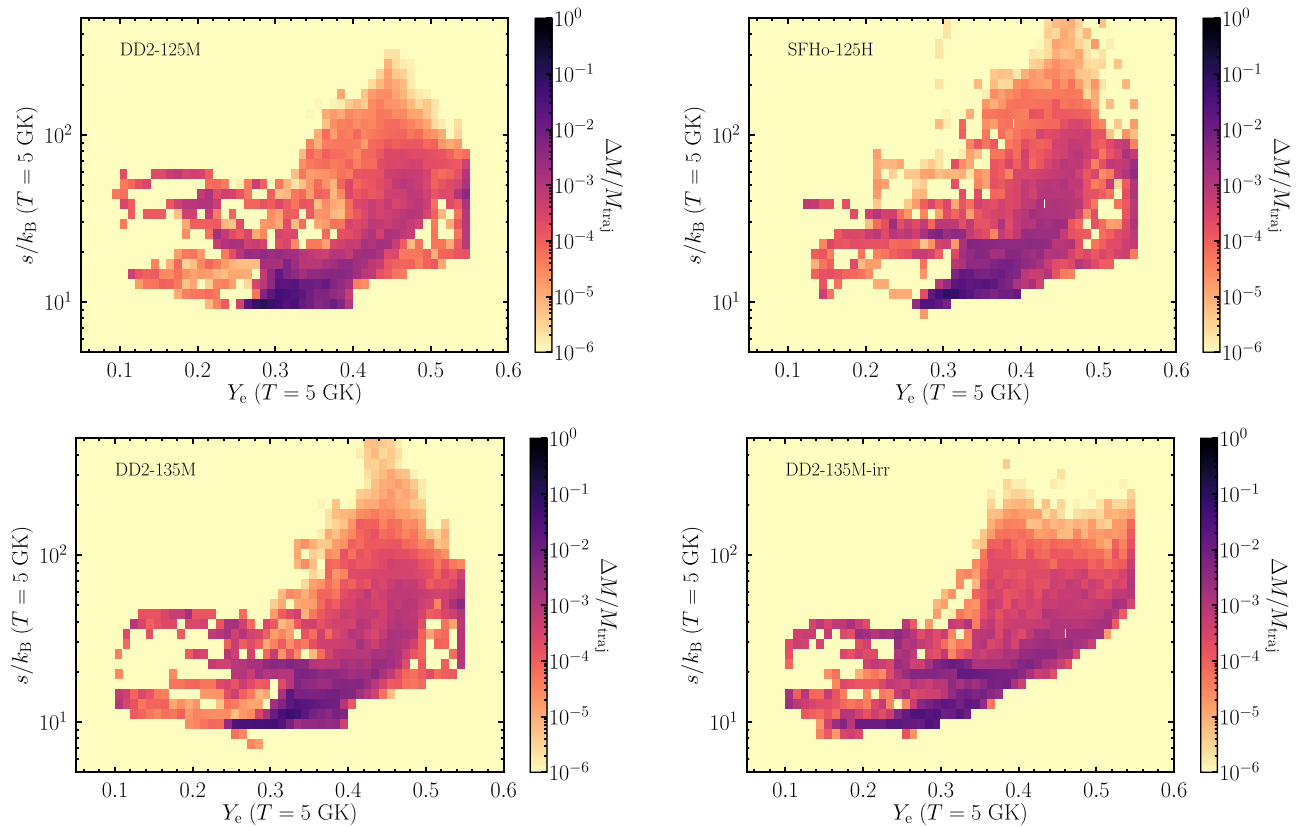
15

Figure 9. Mass distribution of the ejecta in the s–Y_e plane for models DD2-125M (top left), SFHo-125H (top right), DD2-135M (bottom left), and DD2-135M-irr (bottom right). The color code shows the distribution of the mass normalized by the total mass for the tracer particles of each model.

high-optical depth region). This figure illustrates that viscous heating approximately balances out neutrino cooling for $k_B T \gtrsim 1\,\mathrm{MeV}$ (i.e., for the early phase of the evolution), while viscous heating dominates over neutrino cooling for $k_B T \lesssim 1\,\mathrm{MeV}$ (i.e., for the later phase after the neutrino cooling efficiency drops). The late-time viscosity-driven mass ejection occurs in such conditions.

3.4. DD2-125M-h: Higher Viscosity Model

To explore the dependence of the results on the viscous coefficient in particular for the case of extremely high viscosity, we perform a simulation of model DD2-125M-h ($\alpha_{\mathrm{vis}} = 0.1$). In the top-left panel of Figure 11, the ratio of neutrino luminosity to viscous heating rate for model DD2-125M-h is compared to that for model DD2-125M. Due to the faster viscous expansion of the disk, the neutrino cooling efficiency drops and the mass ejection sets in earlier than for DD2-125M. In addition, due to the larger viscous effect, the ejecta mass becomes larger: the total ejecta mass for this model is $M_{\mathrm{ej,tot}} \approx 0.2\,M_\odot$ at the end of the simulation, which is approximately twice as large as that for DD2-125M. The reason for this enhancement is that the viscous timescale is shorter, and hence, a substantial fraction of material is accelerated outward by the neutrino and viscous heating before the material accretes onto the NS.

Due to the earlier mass ejection from the disk, the equilibrium value of the electron fraction at its freeze out ($t \approx 1\,\mathrm{s}$ for DD2-125M-h and $t \approx 2\,\mathrm{s}$ for DD2-125M) becomes lower (Fujibayashi et al. 2020), and thus, the electron fraction of the ejecta becomes lower as well (see the bottom panels of

Figure 11). The bottom-right panel of Figure 11 shows that the mass fraction with low electron fraction ($Y_e < 0.25$) for model DD2-125M-h is remarkably larger than for model DD2-125M.

Figure 12 shows the mass distribution of the ejecta in the s–Y_e plane for model DD2-125M-h. It is clearly found that the ejecta with such low electron fraction is present in the low-entropy ($s/k_B \sim 10$) region. This illustrates that the electron fraction of the ejecta is sensitive to the onset time of the mass ejection. As we discuss in Section 3.5, the mass ejection may proceed in a shorter timescale in the presence of strong magnetic fields. The ejecta mass may be enhanced and the electron fraction of the ejecta may be decreased in the presence of such an efficient mass-ejection process.

3.5. Discussion: Possible Effect of the Magnetic Field in the Postmerger Evolution

The remnant NS and disk formed after the NS mergers would be strongly magnetized due to magnetohydrodynamical instabilities like the Kelvin–Helmholtz instability (Price & Rosswog 2006) and the MRI (Balbus & Hawley 1991), and thus the magnetic field effect could play an important role for determining the ejecta dynamics and the activity of the remnant. In this subsection, we discuss the possible effects of the magnetic field in its presence.

Figure 1 shows that the density in the polar region decreases with time. This indicates that the magnetic pressure by the strong magnetic field would modify the fluid dynamics in such a region. Figure 13 shows the pressure profile for model DD2-125M along the polar direction for $t = 0.01$–$6\,\mathrm{s}$ together with the hypothetical magnetic pressure $P_B = B^2/8\pi$ assuming that
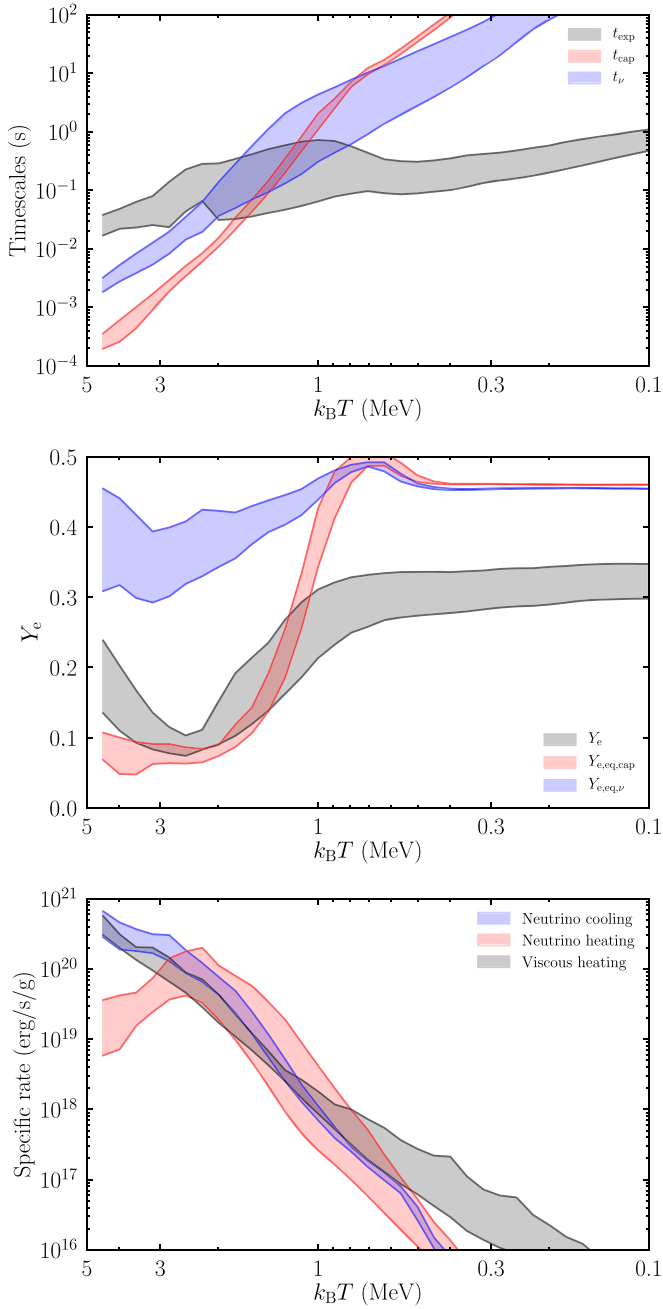
Figure 10. Top: the evolution of the timescales of the tracer particles for the electron (anti)neutrino absorption (blue), electron/positron capture (red), and the expansion of the ejecta (gray) with decreasing temperature (i.e., with the time evolution) for model DD2-125M (see the text for their definitions). Middle: the evolution of the electron fraction (gray), the equilibrium values for neutrino and antineutrino absorption (blue), and electron and positron captures (red) as functions of the decreasing temperature. Bottom: the evolution of the specific heating rate due to the neutrino absorption (red) and the viscosity (gray) as well as the specific cooling rate due to electron and positron capture (blue) as functions of the decreasing temperature. The shaded area indicates the region that contains 50% of the trajectories which have terminal entropy less than $30\,k_B$ around the median of each value.

the magnetic field has a dipole structure with the magnetic strength at the polar surface of the NS as $B_p = 10^{15}$ G. This figure suggests that the pressure along the polar direction substantially decreases after ≈ 0.3 s and that the magnetar-level magnetic field could determine the fluid dynamics along the pole: nearly force-free magnetosphere is likely to be produced.

Using the result of a force-free electromagnetic simulation by Spitkovsky (2006), the electromagnetic luminosity is

$$L \approx \frac{1}{4} B_p^2 R^6 \Omega^4 = 6.6 \times 10^{49} \text{ erg s}^{-1}$$

$$\times \left(\frac{B_p}{10^{15}\,\text{G}}\right)^2 \left(\frac{R_{NS}}{15\,\text{km}}\right)^6 \left(\frac{\Omega}{5000\,\text{rad s}^{-1}}\right)^4. \quad (37)$$

Because the force-free condition would be satisfied only in the polar region, part of this value would be released toward the polar direction. If $\gtrsim 10\%$ of L is released, the long-lived and highly magnetized remnant NS, which should be rapidly rotating, could drive a high-Lorentz factor outflow and be an engine of gamma-ray bursts because the baryon-loading problem is likely to be naturally avoided, and a funnel structure would be helpful for confining the relativistic jet.

Because of the differential rotation of the remnant system, the toroidal magnetic field would be amplified by the winding effect. It would result in the increase in magnetic pressure and the development of a tower-like outflow along the rotational axis (Meier 1999). The electromagnetic luminosity due to this mechanism would be

$$L \sim 10^{50} \text{ erg s}^{-1}$$

$$\times \left(\frac{B}{10^{15}\,\text{G}}\right)^2 \left(\frac{R_{NS}}{10\,\text{km}}\right)^3 \left(\frac{\Omega}{10^4\,\text{rad s}^{-1}}\right) \left(\frac{\delta}{0.1}\right)^3, \quad (38)$$

where $(\delta R_{NS})^3$ is an effective volume for which the magnetic field amplification occurs. At the same time, the material at the polar surface of the NS would be stripped by the strong magnetic field, developing outflow toward the polar direction (Shibata et al. 2011b).

The effective viscosity may not be the only magnetohydrodynamical effect on the disk evolution. If there is a sufficiently strong aligned poloidal magnetic field in the disk, the Lorentz force would expel the disk material, in particular the neutron-rich material located in the region far from the central region, on a shorter timescale than the viscosity. The material ejected by such an effect could be neutron rich if its ejection timescale is short enough for the electron fraction of the material to freeze out earlier (Siegel & Metzger 2018; Fernández et al. 2019; Fujibayashi et al. 2020).

4. Nucleosynthesis

4.1. Nuclear Reaction Network

Nucleosynthetic yields for each tracer particle (Section 2.7) are calculated in a postprocessing step by using a nuclear reaction network code, rNET, as described in Wanajo et al. (2018). The network consists of 6300 isotopes ($Z = 1$–110) that are connected by experimentally evaluated rates when available (JINA REACLIB V2.0,[11] Cyburt et al. 2010; Nuclear Wallet Cards[12]) and those from theoretical models otherwise. Theoretical rates for neutron, proton, and alpha capture (TALYS; Goriely et al. 2008) and β-decay (GT2; Tachibana et al. 1990) are based on a microscopic nuclear-mass prediction (HFB-21; Goriely et al. 2010). Neutrino-induced reactions are not included in the nucleosynthesis calculations, because they are expected to play only minor roles in our present models

---

[11] https://groups.nscl.msu.edu/jina/reaclib/db/index.php
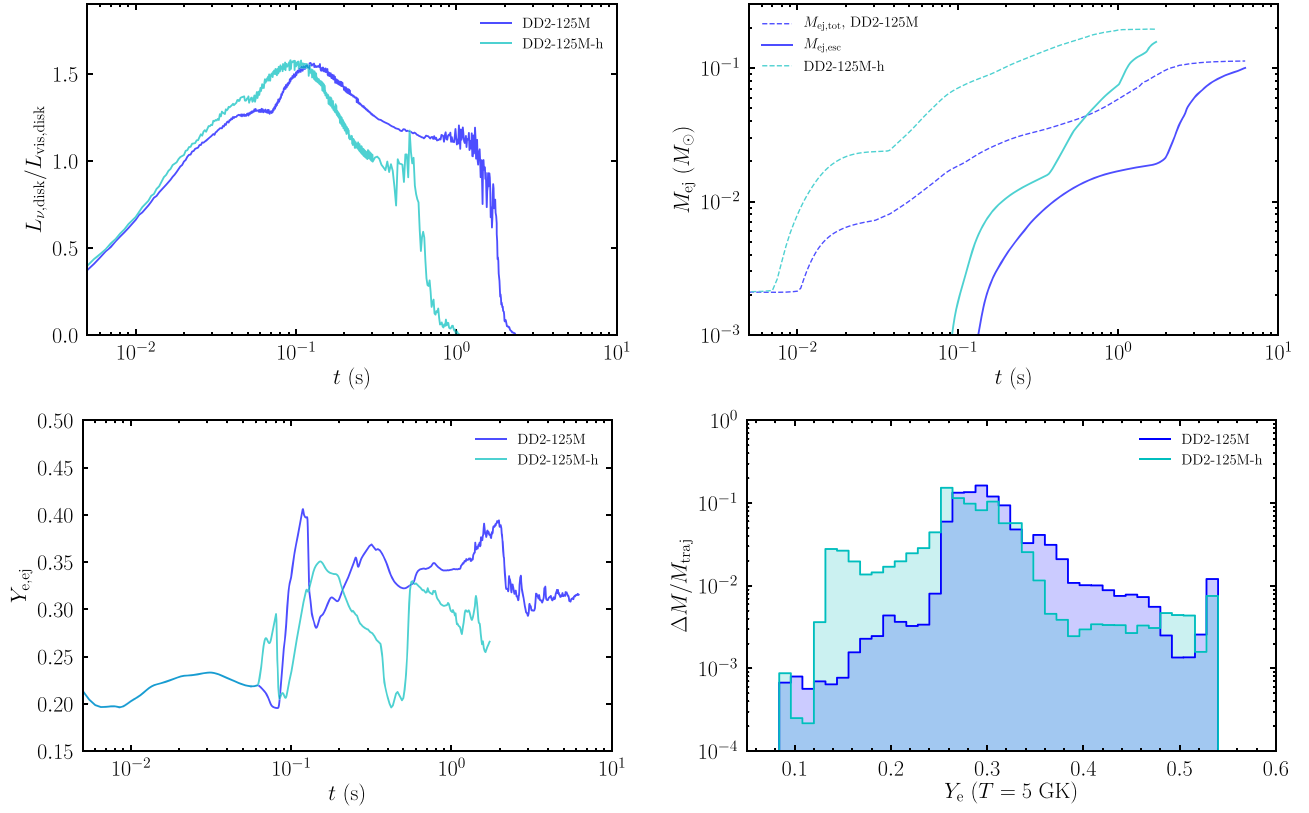[12] http://www.nndc.bnl.gov/wallet/

Figure 11. The ratios of neutrino luminosity to viscous heating rate (top left), ejecta masses (top right), electron fractions (bottom left), and histograms of the electron fraction (bottom right) for models DD2-125M and DD2-125M-h.
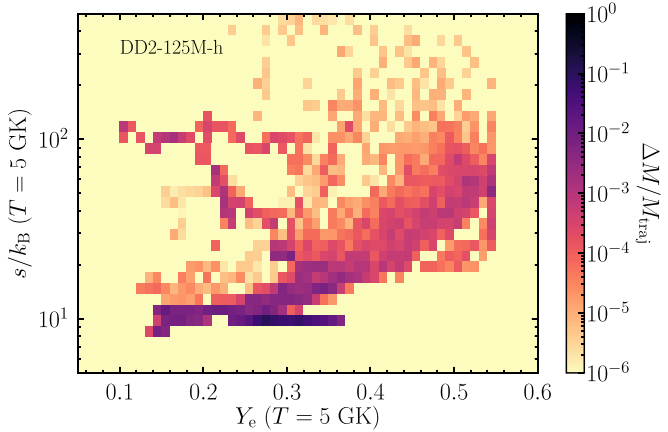

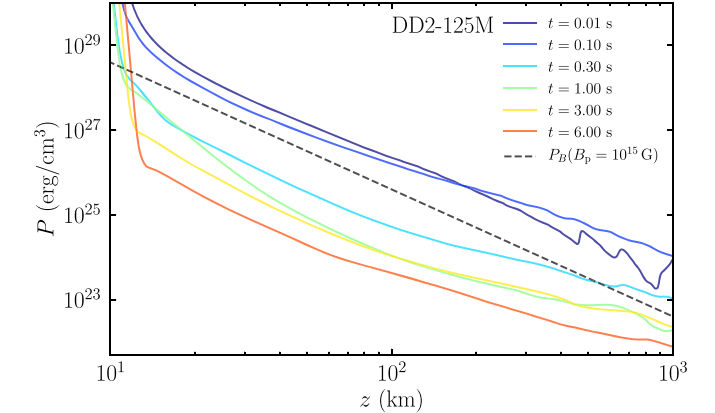**Figure 12.** Mass distribution of the ejecta in the s–Y_e plane for DD2-125M-h.

Figure 13. Pressure profile along the pole of the DD2-125M model at $t = 0.01$, 0.1, 0.3, 1.0, 3.0, and 6.0 s. The magnetic pressure assuming $B_p = 10^{15}$ G is also shown by a dashed line.

(except for setting the values of Y_e at $\gtrsim 10$ GK; see the middle panel of Figure 10).

Each nucleosynthesis calculation starts when the temperature decreases to 10 GK with the initial composition of $1 - Y_e$ and Y_e for free neutrons and protons, respectively. At such high temperature, NSE is immediately established. Although the temperatures in the viscosity-driven ejecta exceed 10 GK, those in the early dynamical ejecta ($\sim 1\%$ of the total amount) already have decreased below 10 GK at ≈ 50 ms (for the 2D cases). For a tracer particle in which the temperature does not reach 10 GK, therefore, the nucleosynthesis calculation starts from the beginning of each postmerger evolution, corresponding to ≈ 50 ms after the merger. The initial composition for such cases is adopted from the nucleosynthesis abundances at 50 ms in the

dynamical ejecta of Wanajo et al. (2014) with (almost) the same initial value of Y_e, because an NSE condition is not assured (in particular for those with <5 GK).

4.2. Nucleosynthesis Yields

The calculated ejecta masses of nucleosynthesis yields for models DD2-125M, DD2-125M-h, SFHo-125H, and DD2-135M are compared in the left panel of Figure 14 (solid lines). Here, the result for DD2-125M-h is added as a limiting case with a large value of $\alpha_{vis} = 0.10$. The r-process residuals to the mass spectrum of the solar system abundances (hereafter the solar r-residuals; Prantzos et al. 2020) are also plotted, which are scaled to fit the ejecta mass of ^{82}Se (one of the first peak
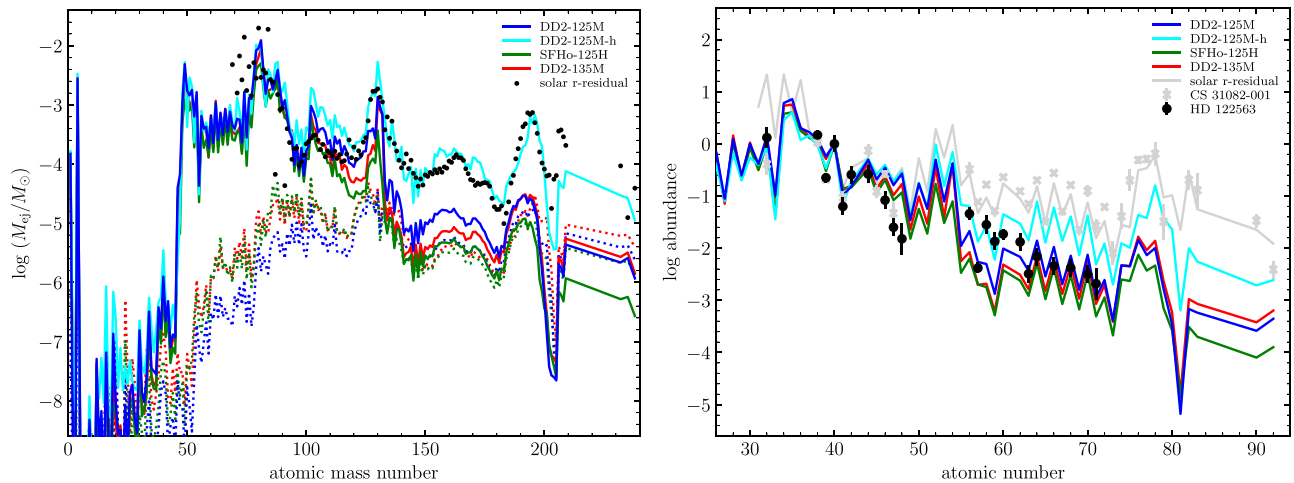
Figure 14. Left: masses (solid lines; in units of $M_\odot$) of nucleosynthesis products at the end of simulation as functions of atomic mass number for models DD2-125M (blue), DD2-125M-h (cyan), SFHo-125H (green), and DD2-135M (red). The solar r-residual masses (Prantzos et al. 2020) are also plotted for comparison purposes, in which the values are shifted to match the mass of ^{82}Se in DD2-135M. The dotted lines with different colors show the masses of dynamical ejecta for corresponding models computed in 3D. Right: comparison of the abundance patterns for the explored models and the stellar abundances of CS 31082–001 (crosses; Siqueira Mello et al. 2013) and HD 122563 (circles; Honda et al. 2006; Ge from Cowan et al. 2005; Cd and Lu from Roederer et al. 2012b). Also plotted is the solar r-residual pattern (gray line, Prantzos et al. 2020). Each abundance distribution is normalized with respect to Zr ($Z = 40$).

abundances) in DD2-125M. Note that our 2D postmerger simulations contain the dynamical ejecta. In fact, the independent nucleosynthesis results (displayed by the dotted lines in the left panel of Figure 14) by using the tracers from corresponding 3D simulations (Table 2) are in reasonable agreement with those from 2D simulations (solid lines, except for DD2-125M-h) for the heavy r-process nuclei ($A > 130$). For DD2-125M, the masses of these nuclei in 2D (blue solid line) are about a factor of a few larger than those in 3D (blue dotted line), indicating that the marginally bound material in the dynamical phase is pushed out by the subsequent early viscosity-driven outflows (Section 3.1). It is interesting to note that the resultant abundance patterns (except for DD2-125M-h) are quite similar to those in the ejecta from BH accretion disks (expected to be formed after massive binary NS mergers) explored in Fujibayashi et al. (2020).

Overall, the abundance patterns are similar among the models with the same viscous parameter (i.e., except for DD2-125M-h), being independent of the NS masses and EOSs adopted. While the abundances lighter than $A = 110$ are in good agreement with the solar r-residual pattern, the heavier nuclei are sizably underabundant (for $\alpha_{\rm vis} = 0.04$). This is a consequence of the fact that the relatively low entropies ($\sim$10–20 $k_{\rm B}$; Figure 7) and mild neutron richness ($Y_{\rm e} \sim$ 0.25–0.5, Figure 8) in the bulk of postmerger ejecta give the nucleosynthesis-relevant conditions for either of NSE, nuclear quasi-statistical equilibrium, or only a weak r-process (e.g., Wanajo et al. 2011, 2018). Conversely, model DD2-125M-h results in the solar r-process-like abundance pattern because of its relatively neutron-rich ejecta ($Y_{\rm e} \sim$ 0.1–0.35; bottom-right panel in Figure 11).

The outcomes for the models with our fiducial choice of $\alpha_{\rm vis} = 0.04$ (DD2-125M, SFHo-125H, and DD2-135M) conflict with the robustness of elemental abundance patterns over a wide range of atomic numbers (in particular for $Z \geqslant 56$ and to a lesser extent for $Z > 38$) among all the r-process-enhanced (or "main" r-process) stars in the Galaxy (e.g., Cowan et al. 2019). In the right panel of Figure 14, the measured abundances of such a star, CS 31081–001 (crosses; Siqueira Mello et al. 2013), are compared with those of our models,

along with the solar r-residual pattern (gray line; Prantzos et al. 2020), which are normalized with respect to Zr ($Z = 40$). We find that the calculated abundance patterns except for DD2-125M-h are rather consistent with those of HD 122563 (circles; Cowan et al. 2005; Honda et al. 2006; Roederer et al. 2012b), one of the r-process-deficient metal-poor stars showing a descending abundance trend and referred to as a "weak" r-process star (Wanajo & Ishimaru 2006). Thus, low-mass NS binaries may be the sources of such weak r-process-like signatures found in metal-poor stars.[13] Alternatively, the viscosity in the disk should be effectively as large as $\alpha_{\rm vis} = 0.10$, which is adopted in DD2-125M-h for reproducing the solar r-process abundance pattern.

As displayed in Figure 15, each model with $\alpha_{\rm vis} = 0.04$ exhibits a solar r-process-like abundance pattern over a wide range of A ($\sim$80–200) only when the time elapsed for the postmerger phase is below 0.2 s. Even if a central remnant collapsed at this epoch (e.g., by the replacement of the binary mass with a larger one or the EOS with a softer one), the subsequent mass ejection from a BH accretion disk would add a substantial amount of material with $A < 130$ as found in Fujibayashi et al. (2020). We conclude, therefore, that the binary NS systems explored in this study, that is, those ejecting small ($\sim$0.001 $M_\odot$) and large ($>$0.05 $M_\odot$) masses in the dynamical and postmerger phases, respectively, cannot be the predominant source of the Galactic r-process material, given that our choice of $\alpha_{\rm vis} = 0.04$ is representative. This implies that the frequency of the low-mass binary NS mergers, leading to long-lived massive NSs as remnants, would be rather low, given that the binary NS mergers were the predominant site of r-process nucleosynthesis. However, if the viscous effect is effectively large with $\alpha_{\rm vis} \sim 0.1$, or in other words, in the presence of an efficient mass-ejection process in the early postmerger phase, this conclusion is significantly modified, as we already mentioned in the previous paragraph.

---

[13] Note that the weak r-process-like stars observed to date exhibit no substantial enhancement of light neutron-capture elements (e.g., having normal Sr/Fe values; Aoki et al. 2017). It is not clear, therefore, if the abundances of such a star represent a single (or a few) nucleosynthesis event.
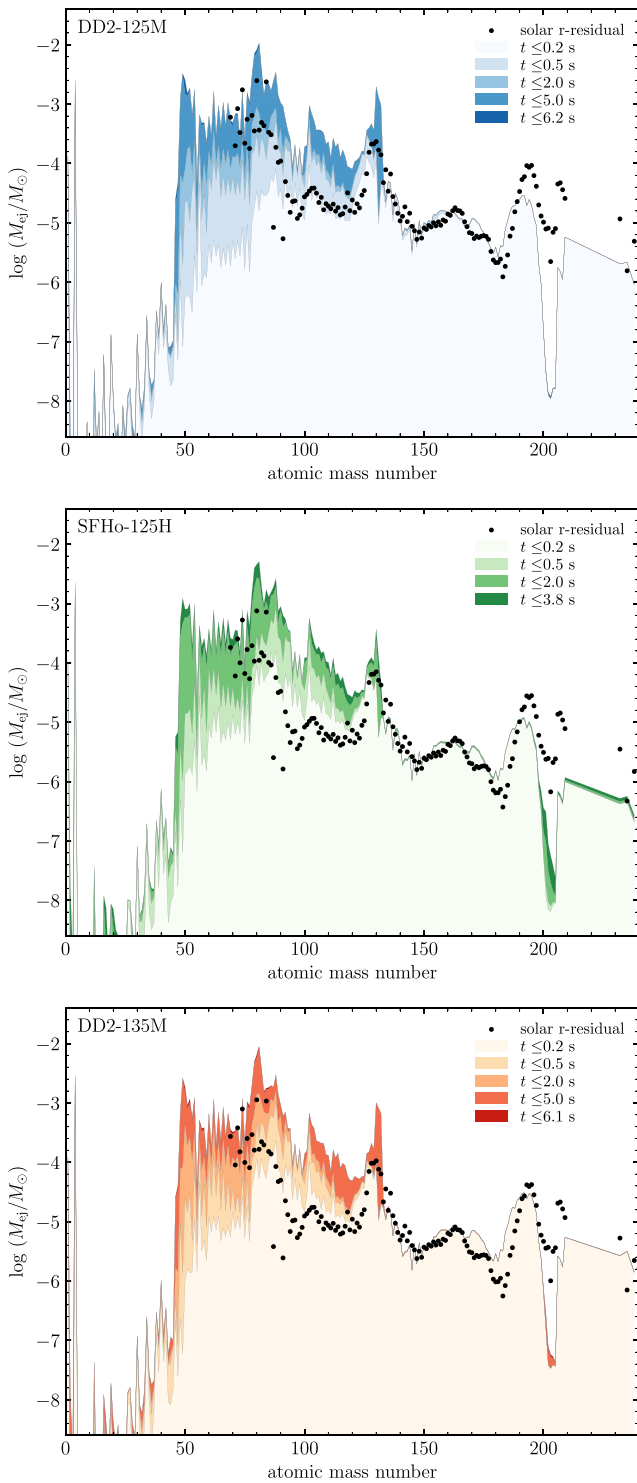
Figure 15. Temporal variation of the ejecta masses (from light to dark colors; in units of $M_\odot$) of nucleosynthesis products as functions of atomic mass number for models DD2-125M (top), SFHo-125H (middle), and DD2-135M (bottom). The solar *r*-residual masses (Prantzos et al. 2020) are also plotted for comparison purposes, in which the values are shifted to match the mass of ^{151}Eu at the end of the simulation.

4.3. Radioactive Energies

We inspect the radioactive decays of the nuclei synthesized in the postmerger ejecta, which give rise to kilonova emission. For this purpose, the nuclear (specific) heating rates ($\dot{q}$; in units

of erg g^{-1} s^{-1}) are computed from the temporal evolution of nucleosynthesis for DD2-125M (blue), DD2-125M-h (cyan), SFHo-125H (green), and DD2-135M (red) as displayed in the left panel of Figure 16 (solid lines). The heating is chiefly due to β-decays; the contributions from fission and α-decays are unimportant except for DD2-125M-h because of the small amount of trans-lead species synthesized in the ejecta (Figure 14). The heating rates for all models resemble each other, in particular for DD2-125M, SFHo-125H, and DD2-135M, because of their similar nucleosynthesis outcomes. However, these deviate from the empirical power-law-like heating (with the index -1.3; dotted line) that has been found in previous studies as a result of the decaying second-peak nuclei ($A \sim 130$) with various half-lives (Metzger et al. 2010; Wanajo et al. 2014).

The reason for this deviation is evident from the right panel of Figure 16 that shows the heating rates from the β-decays of individual isotopes, $\dot{q}_\beta$, which have dominant contributions to the total heating rate, $\dot{q}$ (for DD2-125M as representative). The main contributors are those between the iron group and the first peak nuclei ($A \sim 50$–90) that dominate in the nucleosynthesis yields (Figure 14). Only two second-peak nuclei ($A = 131$ and 132) marginally contribute to the heating rates. Most of these isotopes (listed in Table 4) have half-lives (second column) either of a few hours, a few days, or several tens of days. As a result, these nuclei contribute to heating at different durations, that is, for $t < 1$ day, $t = 1$–10 days, and $t > 10$ days, making three bump-like structures in the curve of $\dot{q}$ (black solid line). For instance, the contributions of the two decay chains ^{66}Ni $\rightarrow ^{66}$Cu $\rightarrow ^{66}$Zn and ^{72}Zn $\rightarrow ^{72}$Ga $\rightarrow ^{72}$Ge with similar half-lives (~ 2 days; Table 4) stand out in the heating rate between 1 and 10 days (as also found in Wanajo 2018; see the discussion on the contribution of various isotopes in different astrophysical conditions in Metzger et al. 2010; Grossman et al. 2014; Lippuner & Roberts 2015; Martin et al. 2015). DD2-125M-h results in a larger heating rate than those in the other models because of the abundant second-peak elements in its ejecta coming into play.

4.4. Comparison with the Kilonova Light Curve of the NS Merger GW170817

The total heating rates, $\dot{Q}$, in the ejecta for each model are calculated as the product of the specific heating rate, $\dot{q}$, the thermalization factor, f_{th}, and the mass of the ejecta, $M_{\text{ej,tot}}$. The thermalization factors for the γ-rays, electrons, α-particles, and fission fragments (the latter two are not shown) are obtained by using the analytic formula in Barnes et al. (2016) with the ejecta mass and the average velocity estimated at the end of the simulation for each model (10th and 11th columns in Table 3), as shown in the left panel of Figure 17. The factors (f_{th}) for γ-rays rapidly decay after several days, while those for electrons slowly decrease at later times (see also Hotokezaka & Nakar 2020). In general, f_{th} is larger for more massive or slowly expanding ejecta. In our models, the average velocities ($\sim 0.1c$) as well as the heating rates are similar to each other, and thus, the ejecta mass is the main source of differences in $\dot{Q}$.

The computed curves of $\dot{Q}$ are compared with the bolometric luminosity of the kilonova (Kasliwal et al. 2017, 2019; Smartt et al. 2017; Waxman et al. 2018) associated with the NS merger GW170817. The right panel of Figure 17 displays the results for models DD2-125M (blue), DD2-125M-h (cyan), SFHo-125H (green), and DD2-135M (red). According to the inferred
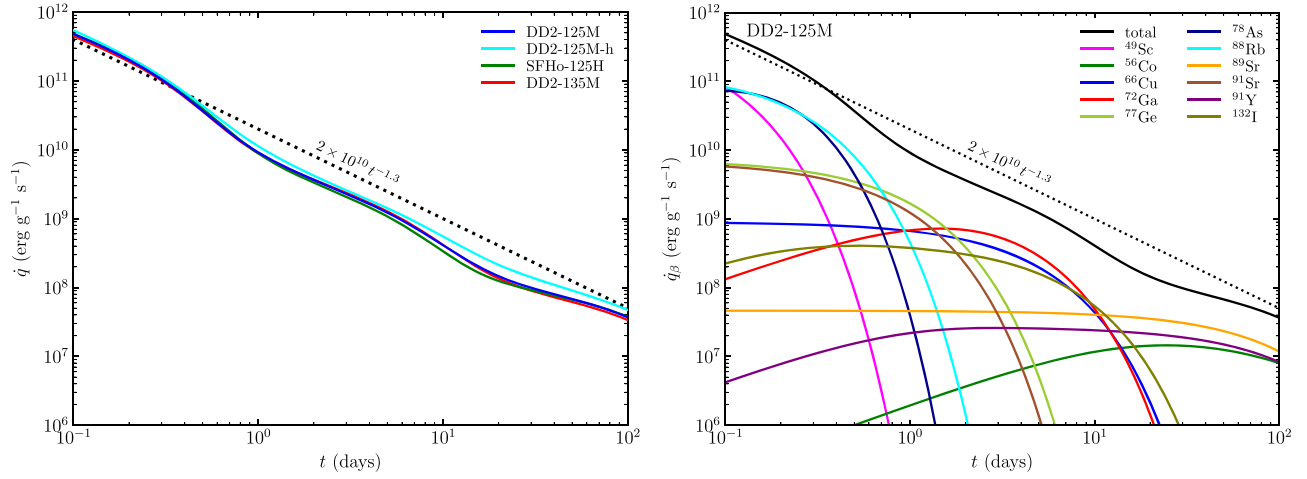
Figure 16. Left: radioactive heating rates, $\dot{q}$ (in units of erg g^{-1} s^{-1}), in the ejecta for models DD2-125M (blue), DD2-125M-h (cyan), SFHo-125H (green), and DD2-135M (red). None of those rates follows the empirical (power-law-type) heating rate indicated by the dotted line. Right: heating rates from the β-decays of individual isotopes, $\dot{q}_\beta$ (in units of erg g^{-1} s^{-1}), for DD2-125M. For readability, only the top 11 isotopes that have more than about 10% contribution at the maxima are displayed in different colors. The black solid and dotted lines indicate the total and the empirical power-law-type rates, respectively.

Table 4
Dominant Decay Chains and Energy Partitions (MeV)[a]

Isotope		Half-life	Gamma-Ray	Electron	Neutrino
^{66}Ni $\rightarrow$ ^{66}Cu		2.27 d	0	0.0733	0.179
	$\rightarrow$ ^{66}Zn	5.12 m	0.0978	1.07	1.48
^{72}Zn $\rightarrow$ ^{72}Ga		1.94 d	0.145	0.0805	0.194
	$\rightarrow$ ^{72}Ge	14.1 h	2.77	0.471	0.759
^{77}Ge $\rightarrow$ ^{77}As		11.3 h	1.08	0.642	0.982
	$\rightarrow$ ^{77}Se	1.62 d	0.00808	0.226	0.448
^{78}Ge $\rightarrow$ ^{78}As		1.47 h	0.278	0.227	0.450
	$\rightarrow$ ^{78}Se	1.51 h	1.31	1.26	1.68
^{88}Kr $\rightarrow$ ^{88}Rb		2.84 h	1.95	0.364	0.606
	$\rightarrow$ ^{88}Sr	17.8 m	0.677	2.05	2.58
^{89}Sr $\rightarrow$ ^{89}Y		50.5 d	0	0.585	0.912
^{91}Sr $\rightarrow$ ^{91}Y		9.63 h	0.707	0.641	0.992
	$\rightarrow$ ^{91}Zr	58.5 d	0.00313	0.603	0.938
^{131}I $\rightarrow$ ^{131}Xe		8.03 d	0.380	0.182	0.396
^{132}Te $\rightarrow$ ^{132}I		3.20 d	0.212	0.0670	0.173
	$\rightarrow$ ^{132}Xe	2.30 h	2.26	0.486	0.837

Note.
[a] Data are taken from the ENDF/B-VII.1 library (Chadwick et al. 2011).

lower bound of the binary mass for GW170817 (2.73 $M_\odot$; Abbott et al. 2017b), the former three should be taken as predictions for future low-mass binary events, while the latter may be taken as representative for this event. In fact, we find that the curve of $\dot{Q}$ for DD2-135M is in good agreement with the observed light curve (different symbols with error bars) between 1 and 10 days, including the bump-like signature at several days after the merger. During this epoch, the radioactive heating is predominantly due to the decay chains from ^{66}Ni and ^{72}Zn, which also is suggested in Wanajo et al. (2018).[14] Despite the heating rate (Figure 16) being about a factor of 2 smaller than the empirical rate (dotted line) expected from a solar r-process-like abundance distribution (e.g.,

Metzger et al. 2010; Wanajo et al. 2014), the large $M_{\rm ej,tot}$ ($=0.086\,M_\odot$) and the subsequent high $f_{\rm th}$ keep $\dot{Q}$ sufficiently high. Conversely, the ejecta masses for the other models are larger or smaller to match the light curve of the merger GW170817. The behaviors of $\dot{Q}$ are, however, similar to each other.

For early times ($t < 1$ days), the radioactive energy has been lost by the adiabatic expansion of the ejecta and thus the heating rate is larger than the bolometric luminosity of the kilonova. During this epoch, the two β-decay chains near the first peak ($A \sim 80$) at the isobars $A = 78$ and 88 (Table 4 and the right panel of Figure 16) play dominant roles in brightening the kilonova emission. It is interesting to note that the identification of the Sr absorption line in the ejecta of the merger GW170817 (Watson et al. 2019) may also be indicative of the contribution of the β-decay chain at $A = 88$ to the luminosity of the kilonova near its peak.

For late times ($t > 10$ days), the main contributors to the kilonova emission are also the isotopes near the first peak (except for DD2-125M-h), as a result of the successive β-decay at the isobars $A = 89$ and 91 (Table 4 and the right panel of Figure 16). The relatively long half-lives of ^{89}Sr (50.5 days) and ^{91}Y (58.5 days) can give rise to the long-lasting kilonova emission. At this epoch, the Spitzer 4.5 μm detection (the right panel of Figure 17; triangles) places a tight lower bound, although the bolometric luminosity itself is highly uncertain. The half-lives of ^{89}Sr and ^{91}Y are similar to that of the spontaneous fission of ^{254}Cf (60.5 days), which is suggested to be a dominant heating source of kilonovae at late times (Wanajo et al. 2014; Hotokezaka et al. 2016; Zhu et al. 2018; Wu et al. 2019). This would make it difficult to confirm the presence of the heaviest r-process nuclei, ^{254}Cf, from the observed kilonova light curves at late times as suggested by Zhu et al. (2018). Note that the decay chain (successive electron capture) of ^{56}Ni $\rightarrow$ ^{56}Co $\rightarrow$ ^{56}Fe (with the half-lives of 6.08 days and 77.2 days) plays a subdominant role to the late-time heating because of their energy deposition exclusively in the form of γ-rays with the diminishing $f_{\rm th}$ for $t > 10$ days (dotted lines in the left panel of Figure 17).

In our explored models, the dynamical ejecta have negligible contributions to the radioactive heating that powers the
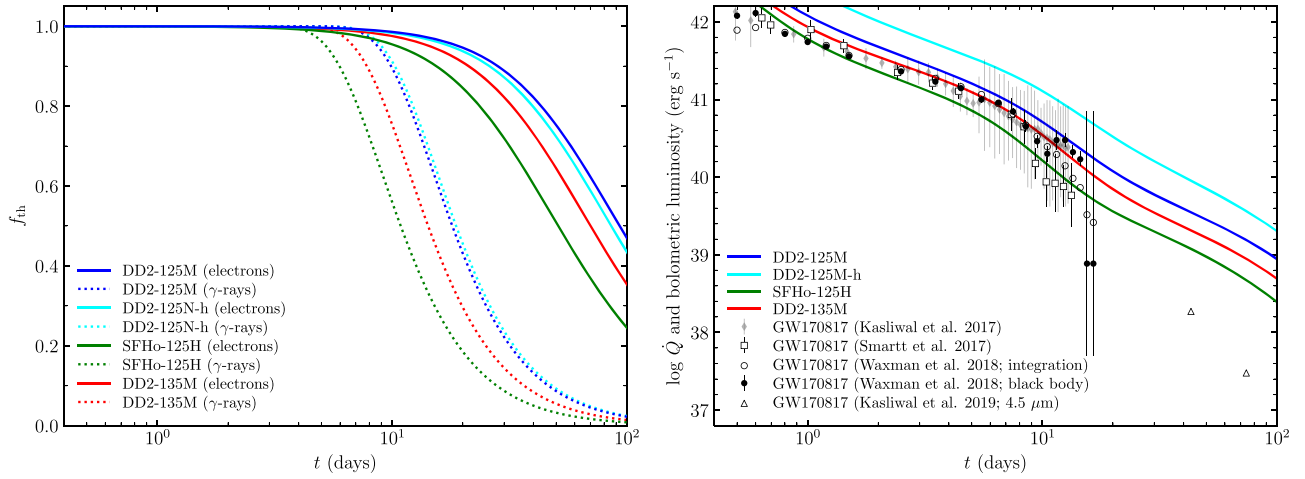
---

[14] The steepening of the light curve can also be due to the fact that the photon diffusion wave crosses the bulk of the ejecta during the first several days (e.g., Hotokezaka & Nakar 2020).

Figure 17. Left: thermalization factors, f_{th}, as functions of time for electrons (solid lines) and γ-rays (dotted lines) using the analytical formula in Barnes et al. (2016) with the ejecta masses ($M_{ej,tot}$) and average velocities ($\langle V_{ej} \rangle$) for models DD2-125M (blue), DD2-125M-h (cyan), SFHo-125H (green), and DD2-135M (red) listed in Table 3. Right: comparison of the total heating rates defined as $\dot{Q} \equiv M_{ej,tot} f_{th} \dot{q}$ (solid lines with different colors) in the ejecta (in units of erg s^{-1}) with the bolometric luminosities adopted from Kasliwal et al. (2017; gray diamonds with error bars), Smartt et al. (2017; open squares with error bars), and Waxman et al. (2018; open circles: integration of the photometric data, filled circles with error bars: blackbody fit to the photometric observation) as well as those at 4.5 μm (i.e., the lower limits; Kasliwal et al. 2019; open triangles) of the kilonova associated with the NS merger GW170817.

kilonova emission. Therefore, the comparison of $\dot{Q}$ with the bolometric luminosity of the kilonova solely does not provide any constraint on the production of heavy r-process elements. However, the mass fraction of lanthanides in each model, X_{la}, serves as another constraint. The values for the models with $\alpha_{vis} = 0.04$, $X_{la} \sim 0.002$–0.004 (last column in Table 3), fall within the observational value, ~ 0.001–0.01, in the kilonova ejecta of the merger GW170817 (e.g., Chornock et al. 2017; Waxman et al. 2018; Even et al. 2020). This indicates that the heavy r-process elements synthesized in the dynamical ejecta become the dominant opacity source of the kilonova, although the amount is insufficient to reproduce the solar r-process-like pattern.

The similar behaviors of the $\dot{Q}$ evolution among our explored models (Figure 17) imply that the low-mass binary events (to be measured in the future) likely exhibit GW170817–like kilonova light curves. The brightness depends, however, on the binary mass as well as the true EOS and viscous parameter.

5. Summary and Conclusions

We explored the postmerger evolution of binary mergers with nearly the lowest mass of double NSs, including the early dynamical mass-ejection phase for self-consistency. Equal-mass binaries with each mass of $1.25\,M_\odot$ (and $1.35\,M_\odot$ for comparison purposes) were explored, in which two different (referred to as "stiff" and "soft," respectively) nuclear EOSs, DD2 (Banik et al. 2014) and SFHo (Steiner et al. 2013), were adopted. For both the dynamical and postmerger phases, we performed general-relativistic numerical simulations with approximate neutrino transport taken into account (Sekiguchi 2010; Fujibayashi et al. 2017).

The early dynamical phase was computed in 3D (K. Kiuchi et al. 2020, in preparation; see also Sekiguchi et al. 2015, 2016). The spatial distributions of physical quantities at ≈ 50 ms were mapped onto the axisymmetric 2D space as the initial condition for the subsequent postmerger evolution using the viscous-hydrodynamics code described in Fujibaya-shi et al. (2017, 2018). The viscous parameter of $\alpha_{vis} = 0.04$

was adopted as a fiducial value and one model of $\alpha_{vis} = 0.10$ was added as a limiting high-viscosity case (DD2-125M-h). The massive NSs survived until the simulations had been terminated (~ 4–6 s after the merger) for our representative models (DD2-125M, SFHo-125H, and DD2-135M). The mass of ejecta (unbound material at the end of simulation) was $M_{ej,tot} = 0.06$–$0.11\,M_\odot$, being about 30% of the initial disk masses as also found in previous studies (Metzger & Fernández 2014; Lippuner et al. 2017; Fujibayashi et al. 2018). The amount of ejecta was larger for a smaller-mass ($1.25\,M_\odot$) binary as well as for a stiffer EOS (DD2) among our models as a result of the larger (initial) disk mass. The overall ejecta properties were found to be similar to each other as characterized by $\langle V_{ej} \rangle/c \sim 0.09$–$0.11$, $\langle s_{ej} \rangle/k_B \sim 15$–$19$, and $\langle Y_{e,ej} \rangle \sim 0.32$–$0.34$. For the high-viscosity model (DD2-125M-h), the ejecta was more massive ($M_{ej,tot} = 0.2\,M_\odot$) as well as more neutron rich ($\langle Y_{e,ej} \rangle \sim 0.28$). This illustrates that the onset time of the mass ejection would be one of the key quantities that characterizes the properties of the ejecta (Fu-jibayashi et al. 2020).

The nucleosynthesis yields were obtained in a postproces-sing step by using $\approx 10,000$–$40,000$ tracer particles deduced from each postmerger model. The resulting abundance trends were similar among all the representative models (DD2-125M, SFHo-125H, and DD2-135M) as anticipated from their ejecta properties. While the early dynamical ejecta were dominated by the heavy r-process nuclei with $A > 130$, the subsequent postmerger ejecta added lighter nuclei at an amount that is an order of magnitude more massive. As a result, the heavier r-process components were sizably underabundant, although the abundance distributions between $A = 80$ and 110 were in reasonable agreement with the solar r-process pattern. Such abundance signatures were in good agreement with those found in weak r-process stars such as HD 122563 (Honda et al. 2006; Aoki et al. 2017). Accordingly, the mass fraction of lanthanides, $X_{la} \sim 0.002$–0.004, is substantially smaller than those in the corresponding early dynamical component (~ 0.07–0.2). By contrast, the high-viscosity model (DD2-

125M-h) resulted in a solar *r*-process-like abundance pattern with a larger amount of $X_{\rm la}$ (~ 0.03) because of more neutron-rich ejecta.

The resultant radioactive heating, an energy source of kilonova emission, was predominantly due to the species between the iron group and first *r*-process peak elements ($A \sim 50$–90), e.g., ^{66}Ni, ^{72}Zn, ^{78}Ge, ^{88}Kr, and ^{89}Sr, rather than those near the second peak ($A \sim 130$) as found in earlier work (e.g., Metzger et al. 2010; Wanajo et al. 2014). The radioactive heating rates did not exhibit a power-law behavior and were a factor of a few smaller than the empirical rate of $\approx 2 \times 10^{10}\, t^{-1.3}$ erg g^{-1} s^{-1} after ~ 1 day. Nevertheless, the total heating rates for 1–10 days were in good agreement (DD2-135M) or even higher (DD2-125M) than the observed luminosity of the kilonova associated with GW170817 because of their large ejecta mass ($0.09\, M_\odot$ and $0.11\, M_\odot$, respectively). Except for the absolute values, the time variations of the total heating rates were similar among our representative models due to a resemblance of their nucleosynthetic outcomes.

The results of our present study as summarized above lead us to several important conclusions. First of all, the long-lived massive NSs with lifetime longer than seconds are the common outcomes of low-mass binary NS mergers. This is confirmed by using stiff (DD2) and soft (SFHo) EOSs, given these EOSs bracketing the properties of the true EOS. Here, we intend "low-mass" binaries to have the system mass of about $2.5\, M_\odot$. This value resides near the lower bound for the observed Galactic NS binaries (e.g., Tauris et al. 2017) such as PSR J1946+2052 ($2.50 \pm 0.04\, M_\odot$, Stovall et al. 2018) as well as that predicted from the theoretical studies of core-collapse supernovae (CCSNe; e.g., Müller 2016; Suwa et al. 2018). As the lowest mass of a single NS obtained from such calculations is $\sim 1.2\, M_\odot$, our assumption of taking equal-mass NSs may be justified.

It is also concluded that the mergers of such low-mass NSs are very rare in reality, given our choice of $\alpha_{\rm vis} = 0.04$ (or less) being realistic, because the nucleosynthetic products in our representative models are dominated only by the light *r*-process nuclei with $A < 100$–130. To date, all the *r*-process-enhanced stars in the Galactic halo (e.g., Cowan et al. 2019) as well as in the ultrafaint dwarf galaxies Reticulum II (Ji et al. 2016), Tucana III (Hansen et al. 2017), and Grus II (Hansen et al. 2020) exhibit the abundance distributions that closely follow the solar *r*-process pattern. Provided that such abundance signatures recorded the nucleosynthetic histories of single NS events (e.g., Ishimaru et al. 2015; Ojima et al. 2018), the majority of NS mergers would also have the solar *r*-process-like abundance distributions in their ejecta. This may exclude the possibility that the binaries resulting from the CCSNe near the low-mass end of progenitors are the main channel for binary NS mergers (e.g., Podsiadlowski et al. 2004).

Although they are expected to be rare, such low-mass NS binaries do exist in the Galaxy as evidenced by the discovery of the double-NS system, J1946+2052 (Stovall et al. 2018). Therefore, the mergers of low-mass NSs may be detected in the future as well. It is expected that the kilonovae of such events share similar properties with those of GW170817, that is, the bright blue emission followed by the fading red component as well as the steepening of the light curve several days after the merger (Waxman et al. 2018). The presence of such Galactic low-mass NS binaries may also imply the future discovery of

stars enhanced with only light neutron-capture elements (i.e., with a high Sr/Fe as opposed to the normal Sr/Fe values in the observed weak *r*-process stars such as HD 122563) by the spectroscopic surveys of metal-poor stars. If the mass ejection is as efficient as that in the model of $\alpha_{\rm vis} = 0.10$, however, the merger may eject a large amount of neutron-rich material, resulting in a solar *r*-process-like distribution. If this is the case, we will observe a bright red emission in the kilonovae. A detailed light-curve prediction for this case will be presented in the forthcoming paper (K. Kawaguchi et al. 2020, in preparation).

It should be noted that future GW170817–like kilonovae cannot necessarily be an indication of low-mass NS merger events; obviously, GW170817, with the total mass of 2.73–$2.78\, M_\odot$ (Abbott et al. 2017a), was not the case. Moreover, our results do not exclude GW170817 being a typical NS merger, although our model DD2-135M (with the total mass of $2.7\, M_\odot$ that is consistent with the lower bound for GW170817) results in similar outcomes to those in DD2-125M and SFHo-125H, which show nonsolar *r*-process abundance patterns. The reasons are that the fate of a merger remnant depends on the nuclear EOS; model SFHo-135 leaves a hypermassive NS immediately collapsing into a BH. We also focus on the equal-mass NS binaries only, which may not be the case for GW170817. The agreement of the total heating rate ($\dot{Q}$) for DD2-135M with the light curve of the kilonova of GW170817 (between 1 and 10 days) does not necessarily indicate the nonsolar *r*-process abundances in the ejecta either. In fact, the solar *r*-process-like ejecta abundances including the first peak (and coproduced ^{66}Ni) can explain the light curve of the kilonova associated with GW170817 (Kawaguchi et al. 2018; Wanajo 2018; Wu et al. 2019).

Finally, we stress that our conclusions presented here are based on the numerical simulations adopting the prescription of the parameterized viscous heating ($\alpha_{\rm vis} = 0.04$ as representative) that drives mass ejection from the accretion disk. As the magnetic turbulence is the predominant source of viscosity in the disk, our results in this study should be testified by a long-term magnetohydrodynamical simulation with a sufficient grid resolution. In addition, the effect of neutrino irradiation on the electron fraction of the ejecta is still uncertain because of our approximate method for neutrino transport. An elaborate treatment of neutrino transport is needed for a more quantitative study. The impact of these effects will be investigated in our future work.

Appendix A
Angular Momentum Loss due to Beamed Neutrino Emission

Here, we estimate the amount of angular momentum loss due to the beamed neutrino emission from the neutrino sphere of the remnant massive NSs with rapid rotation. This effect was already discussed in Baumgarte & Shapiro (1998), but we estimate the loss rate in the general-relativistic momentum formalism (Shibata et al. 2011a).[15]

The source term for the momentum density of the fluid due to neutrino interactions is found in Equation (7.7) in Shibata et al. (2011a) and thus, the evolution of the momentum density of the fluid due to radiation reaction is described by the terms

$$\partial_t(\rho_* h u_i)|_{\rm rad} = -\sqrt{\gamma}\,\alpha S^\mu \gamma_{\mu i}, \tag{A1}$$

where S^μ is the energy-momentum dissipation rate per volume due to the neutrino emission. This is written as

$$S^\mu = \int \frac{d^3 k}{(2\pi)^3} k^\mu B(k) = \int d\omega \frac{\omega^3}{(2\pi)^3} \\ \times \int d\bar{\Omega}(u^\mu + \ell^\mu) B(\omega, \bar{\Omega}), \tag{A2}$$

where B is the so-called collision integral that appears in the Boltzmann equation due to the interaction between radiation and fluid. Note that B includes the emission, absorption, and pair processes, and it is evaluated in the fluid rest frame, so that the momentum of the radiation particle is decomposed as $k^\mu = \omega(u^\mu + \ell^\mu)$ with the energy of the particle in the fluid rest frame $\omega = -k^\mu u_\mu$ and a unit vector ℓ^μ, which satisfies $u^\mu \ell_\mu = 0$. ℓ^μ represents the spatial direction of the momentum of each neutrino in the fluid rest frame and is parameterized by the solid angle $\bar{\Omega}$.

If the angle dependence of the expression in Equation (A2) is small, that is, the source term is nearly isotropic, we obtain

$$S^\mu = u^\mu \int d\omega \frac{\omega^3}{(2\pi)^3} \int d\bar{\Omega} B(\omega, \bar{\Omega}) = u^\mu \dot{Q}_{\rm rad}, \tag{A3}$$

where $\dot{Q}_{\rm rad}$ is the net energy emission rate density. This assumption is valid for the case where the source term is dominated by neutrino cooling due to electron/positron capture or thermal production, which has no preferred direction of the neutrino emission.

We obtain the angular momentum loss rate in a volume V due to neutrino emission by integrating the angular component of Equation (A1) as

$$\frac{dJ}{dt}\bigg|_{\rm rad} = -\int_V d^3 x \sqrt{\gamma}\,\alpha u_\phi \dot{Q}_{\rm rad}, \tag{A4}$$

where we defined the angular momentum in a volume V as

$$J = \int_V d^3 x \rho_* h u_\phi. \tag{A5}$$

By taking the Newtonian limit of this expression as $\gamma = \alpha = h = 1$ and $u_\phi = R^2 \Omega$, where Ω is the angular

velocity, we obtain

$$\frac{dJ}{dt} = -\int_V d^3 x R^2 \Omega \dot{Q}_{\rm rad}$$
$$\approx -R_{\rm NS}^2 \Omega L = -\frac{JL}{\kappa M}$$
$$\approx 6 \times 10^{47} \, {\rm erg \, s^{-1}} \left(\frac{\kappa}{0.4}\right)\left(\frac{J}{10^{49} \, {\rm erg \, s^{-1}}}\right)$$
$$\times \left(\frac{L}{10^{53} \, {\rm erg \, s^{-1}}}\right)\left(\frac{M}{2.6 \, M_\odot}\right)^{-1}, \tag{A6}$$

where $R_{\rm NS}$ is the NS radius and L is the neutrino luminosity, provided that the neutrino sphere is equal to the NS radius. We assumed that the NS would be rigidly rotating and $J = \kappa M R_{\rm NS}^2 \Omega$, where $\kappa M R_{\rm NS}^2$ is the moment of inertia of the NS. This assumption is expected to be valid for $\gtrsim 1$ s after the merger due to its viscous evolution. It is found that the order of magnitude of the angular momentum loss rate agrees with the numerical result presented in Section 3.

Appendix B
Models DD2-135L and DD2-135M-v14

In this appendix, we compare the results of DD2-135L, DD2-135M, and DD2-135M-v14 to investigate the dependence of the grid resolution and the viscous effect inside the NS. First, we focus on the impact of the grid resolution on the results by comparing the models DD2-135M and DD2-135L. The top-left panel of Figure B1 shows that the neutrino luminosity of the NS in DD2-135L starts to deviate from that of DD2-135M at $t \approx 0.3$ s. Even for DD2-135M, the luminosity of NS starts to increase at $t \approx 1$ s. This feature was already found in our earlier work (Fujibayashi et al. 2017), in which the higher resolution model has a lower neutrino luminosity at late times of massive NS evolution. Thus, we would always slightly overestimate the effects of neutrinos in this work. However, as seen in Figures B1 and B2, the average electron fraction and entropy of the disk as well as the quantities related to the ejecta do not change much by increasing the grid resolution. Therefore, we conclude that this spurious increase of the neutrino luminosity does not cause a serious error in evaluating the ejecta properties.

In the top-right panel of Figure B1, we also show the evolution of the angular momentum of the NS. Due to the lower neutrino luminosity for higher resolution models, the decrease of the angular momentum of the NS is slower. Thus, the dissipation of the angular momentum of the NS would be overestimated in this work.

Second, we compare models DD2-135M and DD2-135M-v14, for which the viscosity is switched off in the high-density ($\rho > 10^{14} \, {\rm g \, cm^{-3}}$) region. The mass and other properties of the ejecta agree well with each other for these two models. This indicates that the viscosity inside the NS does not significantly affect the ejecta properties.

The slow increase of the angular velocity inside the NS found even for model DD2-135M-v14 (see the bottom panel of Figure 2) is due to the redistribution of the angular momentum by the fluid motion. To clarify this, we define the increase rate of the average specific angular momentum inside a spherical shell with enclosed mass m, j_m, due to the convective and

---

[15] Neutrino scattering with stellar material could also take angular momentum away (Dvornikov & Dib 2010), but as shown in their work, this effect is limited.
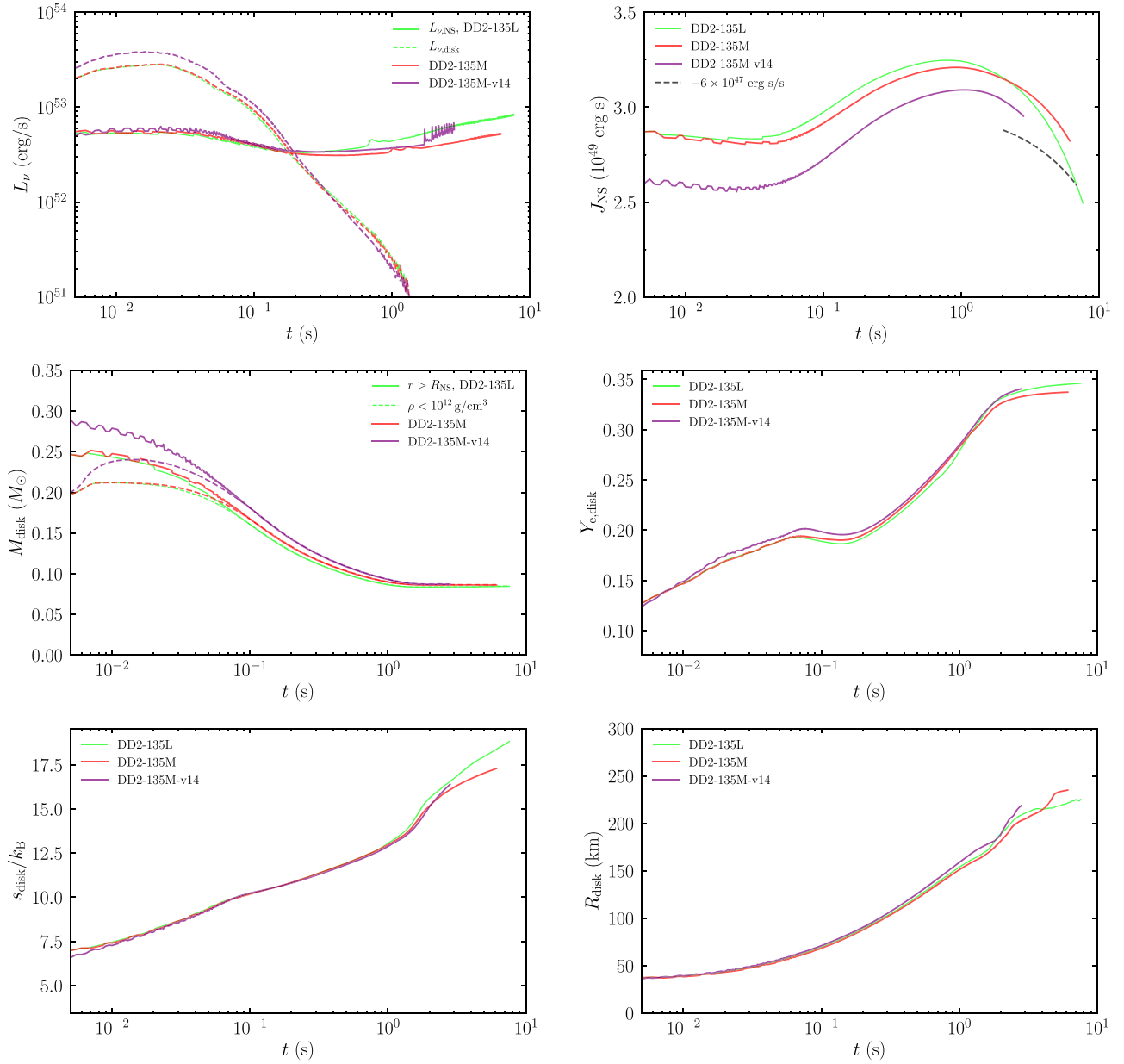
Figure B1. Quantities of the disk and the NS for models DD2-135L, DD2-135M, and DD2-135-v14.

viscous angular momentum transport by

$$\frac{dj_m}{dt} = -\frac{1}{m}\int_{r=r_m} ds\left[\left(v^r - \frac{dr_m}{dt}\right)\rho_* h u_\phi\right.$$
$$\left. + \nu h \rho_* \tau^0{}_{\phi k}\gamma^{kr}\right], \tag{B1}$$

where r_m is the spherical radius of the mass shell, ds is the area element of the sphere with the radius r_m, and dr_m/dt is the radial velocity of the mass shell defined by

$$\frac{dr_m}{dt}\int_{r=r_m} ds\rho_* = \int_{r=r_m} ds\rho_* v^r. \tag{B2}$$

In Figure B3, dj_m/dt and j_m with the mass shell $m = 1.5M_\odot$ as functions of time are shown for models DD2-135M and DD2-135M-v14. The mass shell is located at the radius of ≈ 7 km with the density of $\approx 4 \times 10^{14}$ g cm^{-3}, for which the slope of the angular velocity along the equatorial plane is steepest at $t = 0$

(see the top panel of Figure 2). For model DD2-135M, dj_m/dt has a positive value with the timescale of $j_m(dj_m/dt)^{-1} \sim 10^{-3}$ s for $t \lesssim 0.01$ s due to the viscous angular momentum transport. This timescale is consistent with the viscous timescale inside the NS (see Equation (16)). Then, it becomes negative for $0.01 \text{ s} \lesssim t \lesssim 0.06$ s because of the outward viscous angular momentum transport. The positive value of dj_m/dt for $0.06 \text{ s} \lesssim t \lesssim 0.3$ s is reflected from the spin up of the NS due to the mass accretion from the disk. After the mass accretion becomes weak, dj_m/dt becomes negative again due to the viscous effect. For model DD2-135M-v14, the viscous coefficient ν is zero for the region with $\rho \geqslant 10^{14}$ g cm^{-3}, and thus, the viscous angular momentum transport does not occur at this radius, and thus, the positive value of dj_m/dt is due to the convective angular momentum transport inside the NS. For this case, the timescale is $j_m(dj_m/dt)^{-1} \sim 1$ s at $t \sim 0.1$ s.

Compared to the inviscid model DD2-135M-v0, the increase of the angular velocity for $x \lesssim 10$ km is significant for DD2-
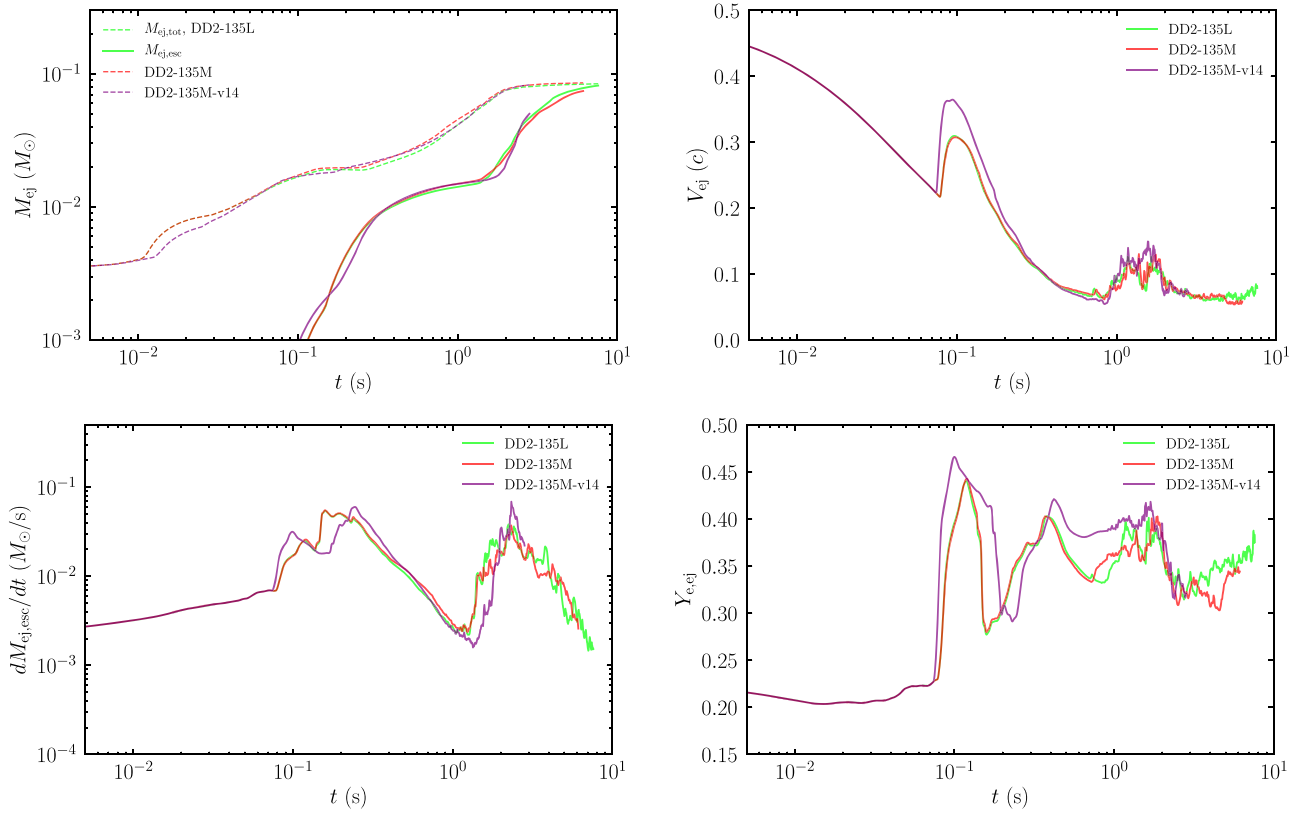
Figure B2. Quantities of the ejecta for models DD2-135L, DD2-135M, and DD2-135-v14.
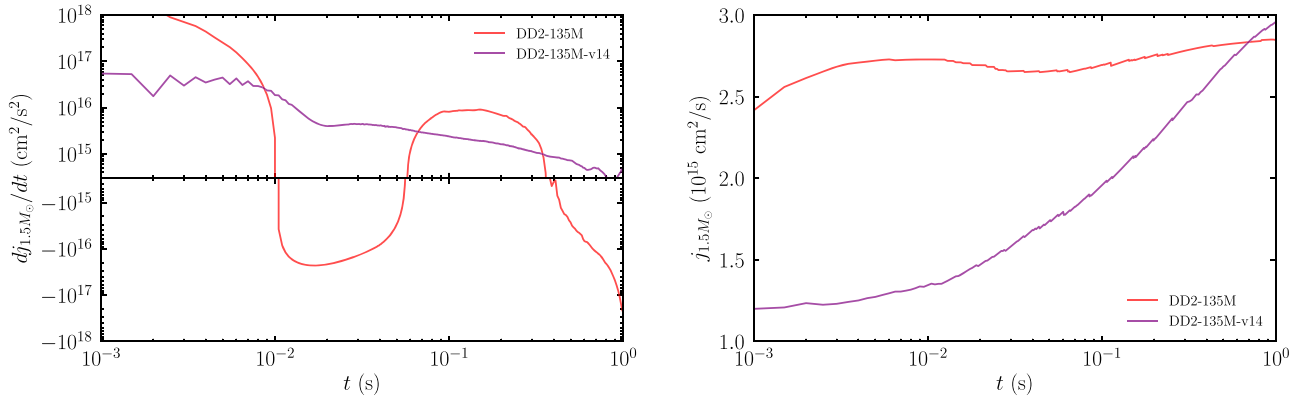

Figure B3. Time evolution of the increase rate of the average specific angular momentum of the material inside the mass shell with $m = 1.5 M_\odot$ (left) and the average specific angular momentum in the region for models DD2-135M and DD2-135M-v14.

135M-v14. Therefore, the convective motion inside the NS would be enhanced by the modification of the stellar structure caused by the viscous effects in the outer part of the NS. Specifically, we speculate that the decrease of the angular velocity and enhanced neutrino cooling at $x \sim 10\,\mathrm{km}$ due to the viscous effect play roles in enhancing the convection inside the NS by weakening the centrifugal force and enhancing the negative entropy gradient in that region.

ORCID iDs

Sho Fujibayashi https://orcid.org/0000-0001-6467-4969
Shinya Wanajo https://orcid.org/0000-0002-4759-7794
Kenta Kiuchi https://orcid.org/0000-0003-4988-1438
Koutarou Kyutoku https://orcid.org/0000-0003-3179-5216
Yuichiro Sekiguchi https://orcid.org/0000-0002-2648-3835
Masaru Shibata https://orcid.org/0000-0002-4979-5671

References

Abadie, J., Abbott, B. P., Abbott, R., et al. 2010, NIMPA, 624, 223
Abbott, B. P., Abbott, R., Abbott, T. D., et al. 2017a, PhRvL, 119, 161101
Abbott, B. P., Abbott, R., Abbott, T. D., et al. 2017b, ApJL, 848, L13
Abbott, B. P., Abbott, R., Abbott, T. D., et al. 2020, ApJL, 892, L3
Accadia, T., Acernese, F., Antonucci, F., et al. 2011, CQGra, 28, 025005
Akutsu, T., Ando, M., Araki, S., et al. 2018, PTEP, 2018, 013F01
Alcubierre, M., Brügmann, B., Holz, D., et al. 2001, IJMPD, 10, 273
Alexander, K. D., Berger, E., Fong, W., et al. 2017, ApJL, 848, L21
Aoki, M., Ishimaru, Y., Aoki, W., & Wanajo, S. 2017, ApJ, 837, 8
Arnowitt, R., Deser, S., & Misner, C. W. 1960, PhRv, 118, 1100
Balbus, S. A., & Hawley, J. F. 1991, ApJ, 376, 214

Banik, S., Hempel, M., & Bandyopadhyay, D. 2014, ApJS, 214, 22
Barnes, J., Kasen, D., Wu, M.-R., & Martínez-Pinedo, G. 2016, ApJ, 829, 110
Baumgarte, T. W., & Shapiro, S. L. 1998, ApJ, 504, 431
Baumgarte, T. W., & Shapiro, S. L. 1999, PhRvD, 59, 024007
Bauswein, A., Goriely, S., & Janka, H. T. 2013, ApJ, 773, 78
Bovard, L., Martin, D., Guercilena, F., et al. 2017, PhRvD, 96, 124005
Chadwick, M. B., Herman, M., Obložinský, P., et al. 2011, NDS, 112, 2887
Chen, W.-X., & Beloborodov, A. M. 2007, ApJ, 657, 383
Chornock, R., Berger, E., Kasen, D., et al. 2017, ApJL, 848, L19
Cowan, J. J., Sneden, C., Beers, T. C., et al. 2005, ApJ, 627, 238
Cowan, J. J., Sneden, C., Lawler, J. E., et al. 2019, arXiv:1901.01410
Cyburt, R. H., Amthor, A. M., Ferguson, R., et al. 2010, ApJS, 189, 240
Dvornikov, M., & Dib, C. 2010, PhRvD, 82, 043006
Eichler, D., Livio, M., Piran, T., & Schramm, D. N. 1989, Natur, 340, 126
Even, W., Korobkin, O., Fryer, C. L., et al. 2020, ApJ, 889, 24
Fernández, R., Foucart, F., & Lippuner, J. 2020, MNRAS, 497, 3221
Fernández, R., & Metzger, B. D. 2013, MNRAS, 435, 502
Fernández, R., Tchekhovskoy, A., Quataert, E., Foucart, F., & Kasen, D. 2019, MNRAS, 482, 3373
Foucart, F., Haas, R., Duez, M. D., et al. 2016, PhRvD, 93, 044019
Freiburghaus, C., Rosswog, S., & Thielemann, F. K. 1999, ApJL, 525, L121
Fujibayashi, S., Kiuchi, K., Nishimura, N., Sekiguchi, Y., & Shibata, M. 2018, ApJ, 860, 64
Fujibayashi, S., Sekiguchi, Y., Kiuchi, K., & Shibata, M. 2017, ApJ, 846, 114
Fujibayashi, S., Shibata, M., Wanajo, S., et al. 2020, PhRvD, 101, 083029
González, M., Audit, E., & Huynh, P. 2007, A&A, 464, 429
Goriely, S., Bauswein, A., Just, O., Pllumbi, E., & Janka, H. T. 2015, MNRAS, 452, 3894
Goriely, S., Chamel, N., & Pearson, J. M. 2010, PhRvC, 82, 035804
Goriely, S., Hilaire, S., & Koning, A. J. 2008, A&A, 487, 767
Grossman, D., Korobkin, O., Rosswog, S., & Piran, T. 2014, MNRAS, 439, 757
Guilet, J., Bauswein, A., Just, O., & Janka, H.-T. 2017, MNRAS, 471, 1879
Hansen, T. T., Marshall, J. L., Simon, J. D., et al. 2020, ApJ, 897, 183
Hansen, T. T., Simon, J. D., Marshall, J. L., et al. 2017, ApJ, 838, 44
Hilditch, D., Bernuzzi, S., Thierfelder, M., et al. 2013, PhRvD, 88, 084057
Honda, S., Aoki, W., Ishimaru, Y., Wanajo, S., & Ryan, S. G. 2006, ApJ, 643, 1180
Hotokezaka, K., Kiuchi, K., Kyutoku, K., et al. 2013, PhRvD, 88, 044026
Hotokezaka, K., & Nakar, E. 2020, ApJ, 891, 152
Hotokezaka, K., & Piran, T. 2015, MNRAS, 450, 1430
Hotokezaka, K., Wanajo, S., Tanaka, M., et al. 2016, MNRAS, 459, 35
Ishimaru, Y., Wanajo, S., & Prantzos, N. 2015, ApJL, 804, L35
Israel, W., & Stewart, J. M. 1979, AnPhy, 118, 341
Janka, H.-T., Hanke, F., Hüdepohl, L., et al. 2012, PTEP, 2012, 01A309
Ji, A. P., Frebel, A., Chiti, A., & Simon, J. D. 2016, Natur, 531, 610
Just, O., Bauswein, A., Ardevol Pulpillo, R., Goriely, S., & Janka, H. T. 2015, MNRAS, 448, 541
Kasliwal, M. M., Kasen, D., Lau, R. M., et al. 2019, MNRAS, in press (doi:10.1093/mnrasl/slz007)
Kasliwal, M. M., Nakar, E., Singer, L. P., et al. 2017, Sci, 358, 1559
Kawaguchi, K., Shibata, M., & Tanaka, M. 2018, ApJL, 865, L21
Kawanaka, N., & Mineshige, S. 2007, ApJ, 662, 1156
Kiuchi, K., Kyutoku, K., Sekiguchi, Y., & Shibata, M. 2018, PhRvD, 97, 124039
Kulkarni, S. R. 2005, arXiv:astro-ph/0510256
Lattimer, J. M., & Schramm, D. N. 1974, ApJL, 192, L145
Levermore, C. D. 1984, JQSRT, 31, 149
Li, L.-X., & Paczyński, B. 1998, ApJL, 507, L59
Liebendörfer, M., Mezzacappa, A., Messer, O. E. B., et al. 2003, NuPhA, 719, C144
Lippuner, J., Fernández, R., Roberts, L. F., et al. 2017, MNRAS, 472, 904
Lippuner, J., & Roberts, L. F. 2015, ApJ, 815, 82
Lyman, J. D., Lamb, G. P., Levan, A. J., et al. 2018, NatAs, 2, 751
Marronetti, P., Tichy, W., Brügmann, B., González, J., & Sperhake, U. 2008, PhRvD, 77, 064010

Martin, D., Perego, A., Arcones, A., et al. 2015, ApJ, 813, 2
Meier, D. L. 1999, ApJ, 522, 753
Metzger, B. D., & Berger, E. 2012, ApJ, 746, 48
Metzger, B. D., & Fernández, R. 2014, MNRAS, 441, 3444
Metzger, B. D., Martínez-Pinedo, G., Darbha, S., et al. 2010, MNRAS, 406, 2650
Meyer, B. S. 1989, ApJ, 343, 254
Miller, J. M., Ryan, B. R., Dolence, J. C., et al. 2019, PhRvD, 100, 023008
Müller, B. 2016, PASA, 33, e048
Nishimura, N., Takiwaki, T., & Thielemann, F.-K. 2015, ApJ, 810, 109
Ojima, T., Ishimaru, Y., Wanajo, S., Prantzos, N., & François, P. 2018, ApJ, 865, 87
Palenzuela, C., Liebling, S. L., Neilsen, D., et al. 2015, PhRvD, 92, 044045
Perego, A., Rosswog, S., Cabezón, R. M., et al. 2014, MNRAS, 443, 3134
Podsiadlowski, P., Langer, N., Poelarends, A. J. T., et al. 2004, ApJ, 612, 1044
Prantzos, N., Abia, C., Cristallo, S., Limongi, M., & Chieffi, A. 2020, MNRAS, 491, 1832
Price, D. J., & Rosswog, S. 2006, Sci, 312, 719
Radice, D., Perego, A., Hotokezaka, K., et al. 2018, ApJ, 869, 130
Roederer, I. U., Lawler, J. E., Cowan, J. J., et al. 2012a, ApJL, 747, L8
Roederer, I. U., Lawler, J. E., Sobeck, J. S., et al. 2012b, ApJS, 203, 27
Sekiguchi, Y. 2010, PThPh, 124, 331
Sekiguchi, Y., Kiuchi, K., Kyotoku, K., & Shibata, M. 2015, PhRvD, 91, 064059
Sekiguchi, Y., Kiuchi, K., Kyotoku, K., Shibata, M., & Taniguchi, K. 2016, PhRvD, 93, 124046
Shakura, N. I., & Sunyaev, R. A. 1973, A&A, 500, 33
Shibata, M. 2000, PThPh, 104, 325
Shibata, M. 2016, Numerical Relativity (Singapore: World Scientific)
Shibata, M., Fujibayashi, S., Hotokezaka, K., et al. 2017a, PhRvD, 96, 123012
Shibata, M., & Hotokezaka, K. 2019, ARNPS, 69, 41
Shibata, M., Kiuchi, K., Sekiguchi, Y., & Suwa, Y. 2011a, PThPh, 125, 1255
Shibata, M., Kiuchi, K., & Sekiguchi, Y.-i. 2017b, PhRvD, 95, 083005
Shibata, M., & Nakamura, T. 1995, PhRvD, 52, 5428
Shibata, M., Suwa, Y., Kiuchi, K., & Ioka, K. 2011b, ApJL, 734, L36
Shibata, M., & Taniguchi, K. 2006, PhRvD, 73, 064027
Shibata, M., Taniguchi, K., & Uryū, K. 2005, PhRvD, 71, 084021
Siegel, D. M., & Metzger, B. D. 2018, ApJ, 858, 52
Siqueira Mello, C., Spite, M., Barbuy, B., et al. 2013, A&A, 550, A122
Smartt, S. J., Chen, T. W., Jerkstrand, A., et al. 2017, Natur, 551, 75
Spitkovsky, A. 2006, ApJL, 648, L51
Steiner, A. W., Hempel, M., & Fischer, T. 2013, ApJ, 774, 17
Stovall, K., Freire, P. C. C., Chatterjee, S., et al. 2018, ApJL, 854, L22
Suwa, Y., Yoshida, T., Shibata, M., Umeda, H., & Takahashi, K. 2018, MNRAS, 481, 3305
Symbalisty, E., & Schramm, D. N. 1982, ApL, 22, 143
Tachibana, T., Yamada, M., & Yoshida, Y. 1990, PThPh, 84, 641
Tauris, T. M., Kramer, M., Freire, P. C. C., et al. 2017, ApJ, 846, 170
Thorne, K. S. 1981, MNRAS, 194, 439
Timmes, F. X., & Swesty, F. D. 2000, ApJS, 126, 501
Villar, V. A., Guillochon, J., Berger, E., et al. 2017, ApJL, 851, L21
Vincent, T., Foucart, F., Duez, M. D., et al. 2020, PhRvD, 101, 044053
Wanajo, S. 2018, ApJ, 868, 65
Wanajo, S., & Ishimaru, Y. 2006, NuPhA, 777, 676
Wanajo, S., Janka, H.-T., & Müller, B. 2011, ApJ, 726, L15
Wanajo, S., Müller, B., Janka, H.-T., & Heger, A. 2018, ApJ, 852, 40
Wanajo, S., Sekiguchi, Y., Nishimura, N., et al. 2014, ApJ, 789, L39
Watson, D., Hansen, C. J., Selsing, J., et al. 2019, Natur, 574, 497
Waxman, E., Ofek, E. O., Kushnir, D., & Gal-Yam, A. 2018, MNRAS, 481, 3423
Woosley, S. E., Heger, A., & Weaver, T. A. 2002, RvMP, 74, 1015
Wu, M.-R., Barnes, J., Martínez-Pinedo, G., & Metzger, B. D. 2019, PhRvL, 122, 062701
Zhu, Y., Wollaeger, R. T., Vassh, N., et al. 2018, ApJL, 863, L23